Spectroscopic Definition of the Biferrous and Biferric Sites in *de Novo* Designed Four-Helix Bundle DFsc Peptides: Implications for O$_2$ Reactivity of Binuclear Non-Heme Iron Enzymes[†]

Caleb B. Bell III,[‡] Jennifer R. Calhoun,[§] Elena Bobyr,[‡,ll] Pin-pin Wei,[‡] Britt Hedman,[‡,ll] Keith O. Hodgson,[‡,ll] William F. DeGrado,*,[§] and Edward I. Solomon*,[‡]

Department of Chemistry, Stanford University, Stanford, California 94305, Department of Biochemistry and Biophysics, School of Medicine, University of Pennsylvania, Philadelphia, Pennsylvania 19104, and Stanford Synchrotron Radiation Laboratory, Stanford University, SLAC, Menlo Park, California 94025

ABSTRACT: DFsc is a single chain *de novo* designed four-helix bundle peptide that mimics the core protein fold and primary ligand set of various binuclear non-heme iron enzymes. DFsc and the E11D, Y51L, and Y18F single amino acid variants have been studied using a combination of near-IR circular dichroism (CD), magnetic circular dichroism (MCD), variable temperature variable field MCD (VTVH MCD), and X-ray absorption (XAS) spectroscopies. The biferrous sites are all weakly antiferromagnetically coupled with μ-1,3 carboxylate bridges and one 4-coordinate and one 5-coordinate Fe, very similar to the active site of class I ribonucleotide reductase (R2) providing open coordination positions on both irons for dioxygen to bridge. From perturbations of the MCD and VTVH MCD the iron proximal to Y51 can be assigned as the 4-coordinate center, and XAS results show that Y51 is not bound to this iron in the reduced state. The two open coordination positions on one iron in the biferrous state would become occupied by dioxygen and Y51 along the O$_2$ reaction coordinate. Subsequent binding of Y51 functions as an internal spectral probe of the O$_2$ reaction and as a proton source that would promote loss of H$_2$O$_2$. Coordination by a ligand that functions as a proton source could be a structural mechanism used by natural binuclear iron enzymes to drive their reactions past peroxo biferric level intermediates.

Carboxylate-bridged binuclear non-heme iron enzymes constitute an expanding class of proteins that perform diverse biological functions involving O$_2$ binding and activation (*1, 2*). Members of this family include ribonucleotide reductase (R2[1] for the diiron containing component), which catalyzes the 1e$^-$ oxidation of an endogenous tyrosine residue (*3*); stearoyl-acyl carrier protein Δ^9-desaturase (Δ^9D), which desaturates fatty acids (*4*); methane monooxygenase (MMOH) (*5*) and the growing subclass of bacterial multicomponent monooxygenases (including toluene monooxygenases, phenol hydroxylase, alkene monooxygenase, as well as others), which hydroxylate various organic substrates; the ferritins, which use iron as a substrate for ferroxidation and iron storage; ruberythrin, which performs peroxidations involving NADH; *myo*-inositol oxygenase (MIOX), which catalyzes the ring-cleaving 4e$^-$ oxidation of its substrate; as well as others. In the majority of these enzymes the diiron sites are housed in four α-helix bundles with a mostly conserved (4 Glu/2 His) protein-derived ligand set. Some minor variations exist; for instance, R2 has a terminal Asp in place of a Glu at position 84 (using the *Escherichia coli* numbering); more diversity is observed in the ligand sets of some ferritins; and in MIOX a fifth helix participates in core housing. The best studied members to date are R2, Δ^9D, and MMOH (*1*). In these proteins, each iron is bound by one terminal carboxylate and one His and bridged by two Glu residues; the bridging Glu and His residues are found in conserved ExxH motifs often used to identify the class. The biferrous site in R2 is described as one four and five coordinate Fe^{II} (4C+5C) weakly antiferromagnetically coupled by two μ-1,3 bridging carboxylates with D84 bound in a monodentate fashion to the 4C center (*6*). The biferrous site in Δ^9D is 5C+5C also

* To whom correspondence should be addressed. W.F.D.: e-mail, wdegrado@mail.med.upenn.edu; phone, 215-898-4590; fax, 215-573-7229. E.I.S.: e-mail, edward.solomon@stanford.edu; phone, 650-723-9104; fax, 650-725-0259.
‡ Department of Chemistry, Stanford University.
§ University of Pennsylvania.
ll Stanford Synchrotron Radiation Laboratory, Stanford University.

[1] Abbreviations: DFsc, due ferro single chain; CD, circular dichroism; MCD, magnetic circular dichroism; VTVH MCD, variable temperature variable field MCD; XAS, X-ray absorption spectroscopy; R2, ribonucleotide reductase subunit; Δ^9D, Δ^9-desaturase; MMOH, methane monooxygenase hydroxylase; NADH, nicotinamide adenine dinucleotide; MIOX, *myo*-inositol oxygenase; 4C, 4-coordinate; 5C, 5-coordinate; 6C, 6-coordinate; VT, variable temperature; ES, excited state; GS, ground state; ZFS, zero-field splitting; *J*, exchange coupling; MOPS, 3-(*N*-morpholino)propanesulfonic acid; NIR, near-infrared; SSRL, Stanford Synchrotron Radiation Laboratory; EXAFS, extended X-ray absorption fine structure; LF, ligand field; O_h, octahedral; T_d, tetrahedral; *D*, axial ZFS parameter; *E*, rhombic ZFS parameter; UV, ultraviolet; FT, Fourier transform.

weakly antiferromagnetically coupled by two μ-1,3 bridging carboxylates (*7*). Crystallography coupled with spectroscopy define the reduced site in MMOH as 5C+5C, but with one μ-1,1 and one μ-1,3 carboxylate bridge that results in weak ferromagnetic coupling of the irons (*7–9*). Additionally, a single H_2O molecule is bound to one Fe^{II} in MMOH (*10, 11*). Of these biferrous cofactor sites in the carboxylate-bridged O_2-activating binuclear non-heme iron enzymes only the 4C+5C site in R2 is poised to react rapidly with dioxygen. Both Δ^9D and MMOH require additional factors for rapid reaction with O_2 (*12*). Addition of substrate-bound acyl carrier protein to Δ^9D promotes conversion to a 4C+5C reactive site, and addition of component B to MMOH forms a new 5C+5C site that rapidly reacts with O_2 (*7*).

Parallels among the oxygen reactions of these and other binuclear non-heme iron enzymes are often made, in particular involving spectroscopically, therefore, structurally similar peroxo-biferric intermediates (*1, 4, 13–18*). However, due to different late intermediates (i.e., the Fe^{III}-μ-O/μ-OH-Fe^{IV} intermediate X (*19, 20*) in R2 and the proposed Fe^{IV}-bis μ-O-Fe^{IV} intermediate Q (*21, 22*) of MMOH) and final reaction outcomes, their mechanisms diverge. This is generally believed to occur subsequent to the peroxo species; however, specific factors which stabilize peroxo level intermediates and channel them toward different reaction pathways remain largely unknown. Considerable insight has come from top-down approaches involving site-directed mutagenesis on the native enzymes. Characterization of numerous mechanistically important R2 variants, notably some involving the D84E amino acid substitution which stabilizes the peroxo adduct, have allowed detailed mechanistic dissection of the R2 reaction coordinate which is perhaps the most well defined experimentally of the binuclear non-heme enzymes (*16, 17, 20, 23–28*). Alternatively, for MMOH a genetic system is not yet available, and research has focused on computational and biomimetic model complexes for mechanistic insight (*21, 29–33*).

High valent analogues of Q and X have been generated (*34*), notably an $Fe^{IV}(\mu$-O$)_2Fe^{IV}$ model for intermediate Q that is competent in H-atom abstraction from 9,10-dihydroanthracene (*33, 34*). A number of ligand systems have been shown to support peroxo level species (*34*), and a recent achievement is the synthesis of a peroxo-diiron complex in which reactivity can be tuned to either reversible dioxygen binding or arene hydroxylation by the bridging carboxylates (*35*). Additionally, inorganic model complexes have been indispensable in development of methodologies required for the study of binuclear non-heme enzymes (*34, 36, 37*). The inorganic analogue approach, however, is somewhat limited as the model systems often have only loosely related ligand sets, lack hydrophobic active site environments or second shell interactions provided by the protein, undergo dimerization or disproportionation side reactions, and typically do not offer systematic variability (*34*).

Developments in *de novo* design have created a bridge between small inorganic models and native proteins which incorporates most of the benefits of both experimental approaches (*38–43*). The DF (due ferro) family of rationally designed peptides isolate the diiron site in four-helix bundles and are minimal mimics of the natural binuclear enzymes. The diiron site is coordinated by two tandem helical ExxH motifs and two additional terminal Glu residues. These
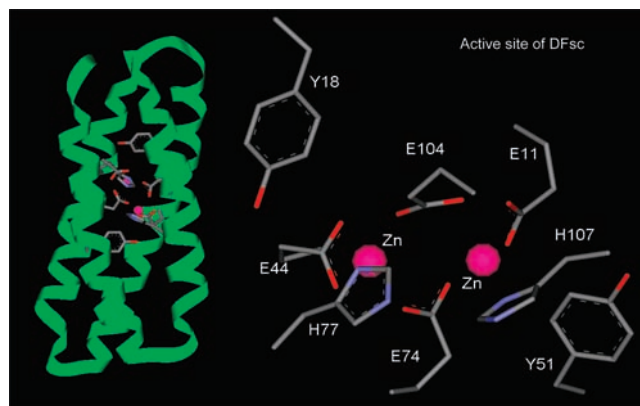

FIGURE 1: Cartoon diagram of the protein fold and active site NMR structure of diZn^{II} reconstituted DFsc (PDB ID 2HZ8).

peptides replicate the coordinating residues of the native enzymes and provide a scaffold for systematic variation of amino acids (*44*). The DFsc peptides are easily generated and available in pure, homogeneous, and highly concentrated samples, making them amenable to detailed spectroscopic investigations. Furthermore, they bind divalent transition metals and react with dioxygen when reconstituted with Fe^{II} reminiscent of the O_2 reactivity of the binuclear non-heme iron enzymes (*45–47*). These designed peptides allow a ground-up molecular biology/spectroscopy approach to define the factors that tune diiron sites for differential oxygen reactivity not directly available in either the proteins or the inorganic models.

Since the initial design of DF1 (*39, 40, 48*), various generational improvements on the scaffold have been made including increasing solubility and access to the active site (*43*). The current generation of single chain DF peptides (DFsc) reacts rapidly with dioxygen when reconstituted with Fe^{II} to form spectroscopically observable species (*49*). Figure 1 shows the overall fold and active site (along with residues pertinent to this study) determined from the diZn^{II} NMR structure of DFsc (*47*). DFsc and the conservative coordinating residue variant DFscE11D react with dioxygen to form a species with a maximum absorption at 520 nm that has been shown by resonance Raman spectroscopy to derive from coordination of a single tyrosine to Fe^{III}, and VT MCD shows this site is a weakly antiferromagnetically coupled $S = 0$ biferric site (*49*).

In this study, the biferrous sites of DFsc, DFscE11D, DFscY51L, and DFscY18F are spectroscopically defined using a combination of circular dichroism (CD), magnetic circular dichroism (MCD), variable temperature variable field MCD (VTVH MCD), and X-ray absorption spectroscopies (XAS). The E11 $\rightarrow$ D substitution was found to stabilize the 520 nm tyrosine-bound biferric species, and this has been further probed by XAS. Single Y variants of DFsc have been generated to determine which residue is responsible for the 520 nm feature and investigate the influence of second shell amino acids on the diiron site. DFscY51F and DFscY18L were also been generated; a Y to F substitution is more conservative than Y to L though the Stokes radius of L is similar to Y. Experimental complications (heterogeneity and concentration) preclude detailed spectral analysis of DFscY51F. Biferrous sites are spectroscopically inaccessible to traditional physical methods such as UV/vis and EPR, due to the parity forbiddenness of d $\leftarrow$ d transitions and their integer spin

ground states. CD and MCD spectroscopy have different selection rules than absorption spectroscopy, and at low temperatures ferrous d ← d transitions become intense in MCD, probing the excited states (ES) of the metal ions thus allowing definitive coordination number and geometric assignments (*1, 50*). The VTVH MCD method uses an excited state to interrogate the ground state (GS) and yields information about the zero field splitting (ZFS) and exchange coupling (*J*) of the diiron system (*50*). ZFS provides geometric and electronic information complementary to CD/MCD, and the sign and strength of the exchange coupling are diagnostic of possible bridging moieties and coordination modes at the biferrous site. Analysis of XAS data provides information about oxidation state and geometric structure. Together, these spectroscopic studies elucidate the nature of the biferrous and biferric sites in these *de novo* designed peptides and provide insight into their reactivity with O_2.

MATERIALS AND METHODS

Sample Preparation. MOPS buffer (Sigma), sodium chloride (Sigma), ferrous ammonium sulfate hexahydrate (Mallinckrodt), deuterium oxide (99.9 atom % D; Aldrich), sodium dithionite (Sigma), and glycerol (98% D; Cambridge Isotope Laboratories) were used as obtained. All anaerobic manipulations were performed under a N_2 atmosphere in a glovebox. Deuterated buffer was degassed with 99.9% argon; glycerol was degassed by heating under vacuum overnight followed by 10+ freeze−pump−thaw cycles at 10^{-3} Torr. DFsc and variants were expressed and purified as previously reported, and all experiments were performed at pH = 7.0 (pD = 7.4) unless otherwise noted (*47, 51*). Protein concentrations were determined by using the molar extinction coefficient at 280 nm (ϵ = 8250 mM^{-1} cm^{-1} for DFsc and DFscE11D and 6970 mM^{-1} cm^{-1} for the single Y variants). For CD/MCD measurements, buffer exchange was carried out by adding deuterated buffer to the sample and concentrating to 2−3 mM. This process was repeated until the percentage of D_2O was greater than 99.9% of the solvent. The protein samples were prepared and loaded into the sample holders under an inert atmosphere. The procedure for Fe^{II} loading into the apoprotein under anaerobic conditions has been previously described (*23*). To the anaerobic Fe^{II}-loaded protein samples, 2 μL of 5 mM methyl viologen and 2 μL of 10 mM dithionite were added to ensure anaerobic conditions during the collection of CD spectra. Protein samples were prepared for MCD in the same way as for CD, with an additional step of mixing the protein with 60% (v/v) glycerol-d_6 until homogeneous to create a suitable glass. From CD studies, glycerol was found to have no effect on the biferrous site. The samples were loaded into MCD cells and immediately frozen in liquid nitrogen.

UV/Vis Absorption. All reactions were performed at 25 °C, in 150 mM MOPS and 150 mM NaCl, pH 7.0. Final protein concentrations were 100 μM and 200 μM iron. An anaerobic ferrous ammonium sulfate solution was added to the protein, mixed, and allowed to equilibrate for 30 min prior to loading into the stopped-flow instrument. Absorption kinetics with ~2 ms dead time were obtained using an Applied Photophysics SX.18MV stopped-flow spectrophotometer equipped with a Hg/Xe arc lamp and outfitted with PEEK tubing. The tubing, plungers, and valves of the

stopped-flow instrument were made anaerobic by washing with dithionite solution followed by several washes with degassed buffer. O_2 exposure was prevented by a stream of N_2 gas through the system. The cell path length was 1 cm, and the temperature was maintained using a water bath. The kinetic data for the variants were modeled as in previous studies on "wild-type" and DFscE11D peptides (*49*). Rate constants quoted in the text are the average of fits from three sets of independent data.

CD and MCD Spectroscopy. Near-IR (NIR) CD studies were performed on a JASCO J200D spectropolarimeter operating with a liquid nitrogen cooled InSb detector in the 560−2000 nm region. Low-temperature MCD and VTVH MCD data were acquired on this spectropolarimeter, modified to accommodate an Oxford Instruments SM4000 7-T super-conducting magnet capable of magnetic fields up to 7.0 T and temperatures down to 1.6 K. Protein samples prepared for MCD studies were slowly inserted into the cryostat to reduce strain in the resulting optical glass. The CD and MCD spectra were fit using a constrained nonlinear least-squares procedure in order to find the minimum number of ligand field transitions required to simultaneously fit both spectra. CD spectra were collected at 4 °C, and MCD spectra were obtained at 5 K; thus in the fitting procedure bands were allowed to sharpen and shift slightly (<300 cm^{-1}) in MCD relative to CD. VTVH MCD (MCD intensity as a function of temperature and applied magnetic field) data were collected at two wavelengths for DFsc, DFscE11D, and DFscY51L. Data were obtained at ~1.8, 3, 5, 7.5, 10, 15, 20, and 25 K and 0, ±0.35, ±0.7, ±1.4, ±2.1, ±2.8, ±3.5, ±4.2, ±4.7, ±5.6, ±6.3, and ±7.0 T for each temperature. Reported data points represent the average of 200−600 scans at each temperature and field (averaging positive and negative). All of the VTVH MCD curves reported here are plotted as a function of $\beta H/2kT$. The data were fit using methods previously developed (*23, 45, 50, 52*). The doublet method uses a series of non-Kramers doublets and/or singlets in a simplex routine that minimizes the χ^2 value to simulate the VTVH MCD data (*50*). The spin Hamiltonian model fits the VTVH MCD data directly to the Hamiltonian and is described in the Results section (*52*).

X-ray Absorption Spectroscopy (XAS). The reduced XAS samples were prepared under the following conditions: 2.5 mM DFsc in 150 mM MOPS, pH 7, 2.0 mM sodium dithionite, and 40% glycerol; 2.8 mM DFscE11D, 150 mM MOPS, pH 7, 2.4 mM sodium dithionite, and 40% glycerol; and 2.8 mM DFscY51L, 150 mM MOPS, pH 7, 6.3 mM sodium dithionite, and 50% glycerol. The oxidized DFscE11D XAS samples contained 2.5 mM protein, 150 mM MOPS, pH 7, and 40% glycerol and were frozen in liquid nitrogen after 20 s of incubation with O_2. For each sample, ~100 μL of solution was transferred into a Lucite XAS cell with 37 μm Kapton tape windows in an inert atmosphere and then frozen in liquid nitrogen. The X-ray absorption spectra were recorded at the Stanford Synchrotron Radiation Laboratory (SSRL) on focused 16-pole wiggler beam line 9-3 with the ring operating at 3 GeV, 80−100 mA. A Si(220) double-crystal monochromator was utilized for energy selection at the Fe K edge, and a Rh-coated mirror upstream of the monochromator was used for harmonic rejection. The samples were maintained at 10 K during data collection by using an Oxford Instruments CF1208 continuous-flow liquid

helium cryostat. Data were measured in fluorescence mode as Fe Kα fluorescence by using a Canberra (Meriden, CT) 30-element solid-state Ge array detector. The internal energy calibration was performed by simultaneous measurement of the absorption of Fe foil placed between two ionization chambers filled with N_2 located after the sample. The first inflection point of the foil was assigned to 7111.20 eV. No photodegradation was observed for the reduced samples. For oxidized DFscE11D, a gradual decrease in the energy of the edge region and slight changes in the EXAFS were observed upon continuous scanning at the same spot. Hence, four distinct and physically separate spots on the three XAS samples were exposed, and only first scans at each spot were used for data analysis. The averaged data included 25 scans for reduced DFsc, 26 scans for reduced DFscE11D, 29 scans for reduced DFscY51L, and 12 scans for oxidized DFscE11D.

The averaged data were normalized with the program XFIT (*53*) by first subtracting a polynomial background absorbance that was fit to the pre-edge region and extended over the post-edge with control points, followed by fitting a three-region polynomial spline of orders 2, 3, and 3 over the post-edge region. The data were normalized to an edge jump of 1.0 between the background and spline curves at 7130 eV. Theoretical EXAFS signals $\chi(k)$ were calculated using FEFF (version 7.02) (*54*) and fit to the nonfiltered data by EXAFSPAK. The input structure for FEFF was revised according to the fit results obtained. The experimental energy threshold, E_0, the point at which the photoelectron wave vector $k = 0$, was chosen as 7130 eV and was varied in each fit using a common value for every component in the fit. The scale factor, S_0^2, was set to 1.0. The structural parameters that were varied during the refinements included the bond distance (R) and the bond variance (σ^2). Atom types and coordination numbers were systematically varied during the course of the analysis but were not allowed to vary within a given fit. Data were fit over the k range of 2−15 Å^{-1} for biferrous DFsc, DFscY51L, and DFscE11D and 2−13 Å^{-1} for oxidized DFscE11D. Fourier transforms of the EXAFS data were calculated with EXAFSPAK.

The intensities and energies of the pre-edge features for all samples were quantified by using the fitting program EDG_FIT and previously established methodology (*55*). All spectra were fit over several energy ranges (7108−7116, 7108−7118, and 7108−7119 eV), with varied backgrounds to give 9−15 fits per sample. Each pre-edge feature was modeled with pseudo-Voigt line shapes of a fixed 1:1 ratio of Lorentzian to Gaussian contributions. The optimal backgrounds were chosen to give a best fit to the pre-edge area while reproducing edge features. Each fit was considered successful if it simultaneously reproduced the data and the second derivative of the data over the entire energy range. The total area is the sum of the areas of all pre-edge features, where the area is approximated by the peak height multiplied by the full width at half-maximum, scaled by 100. Error was calculated by determining the standard deviation for peak heights and half-widths for each pre-edge feature from all successful fits.

RESULTS

CD/MCD Spectroscopy. Anaerobic Fe^{II} titrations, monitored by CD spectroscopy, for DFsc and the E11D, Y51L,

and Y18F variants show saturation behavior for iron uptake maximizing with 2 equiv of Fe^{II} per peptide (K_d's for iron binding are estimated at less than 100 μM, Figure S1). Previously, it was suggested that the rate of iron loading into DFscE11D was considerably slower than for DFsc (*49*). Since the dissociation constants for Fe^{II} are similarly low, this must reflect kinetic control of iron access. The fully loaded biferrous peptides each exhibit highly similar NIR CD spectra at 4 °C (Figure 2, top). The CD and MCD of DFscY18L were collected and shown in Figure S2; however, they are identical to DFscY18F, and the more conservative variant was used for analysis. Each spectrum is composed of one positive low-energy feature at ∼5500 to 6000 cm^{-1} (note that spectra were not collected below 5000 cm^{-1} due to instrument limitations and interference by D_2O vibrations) and a broader asymmetric negative feature with an intensity maximum around 9000 cm^{-1} that can be resolved into two bands. MCD spectra (Figure 2, bottom) were collected at low temperature and are composed of two positive higher energy transitions in the 7000 to 9500 cm^{-1} that vary in intensity across the series and one weak low-energy negative transition (in the MCD spectrum of DFsc, DFscE11D, and DFscY18F, but not DFscY51L, this feature changes sign with positive and negative field directions confirming that these are weak electronic transitions, not baseline effects). Figure 2 shows simultaneous Gaussian resolution of the CD and MCD spectra. Both spectroscopies have different selection rules; thus transitions can have different intensities and signs but must have similar energies. A minimum of three transitions, between ∼10000 and 5500 cm^{-1}, are required to well reproduce the CD and MCD spectra for each DF variant. The presence of three transitions reflects two inequivalent ferrous ions in the active site, as one ferrous center can only give rise to two d ← d transitions in this spectral region (*56, 57*).

A CD/MCD methodology has been developed to correlate spectra with site geometry (*1*). Fe^{II} in a 6-coordinate (6C) geometry has two MCD transitions around 10000 cm^{-1} split by 2000 cm^{-1}. Square pyramidal (5C) sites display one d ← d transition above 10000 cm^{-1} and one in the 5000 cm^{-1} region; these are lowered in energy on going to a trigonal bipyramidal geometry (*50*). Tetrahedral (4C) sites show only low-energy ligand field (LF) transitions, since $10Dq_{(T_d)} = -^4/_9(10Dq_{(O_h)})$ (*50*).

The spectrum of DFsc is resolved into three LF transitions at 5940, 7960, and 9380 cm^{-1} (all values quoted in the text are from MCD data, unless otherwise noted). The CD and MCD spectra of the variants are very similar, suggesting they have similar excited states, and the results of simultaneous resolution of the CD and MCD spectra are summarized in each panel of Figure 2 and Table 1. Notably, the Y51L variant shows a significant red shift of ∼550 cm^{-1} of the 7960 cm^{-1} band in DFsc. In all of these DFsc peptides, features characteristic of 6C iron (i.e., two higher energy transitions) are not observed. The presence of a transition at greater than 8000 cm^{-1} requires at least one iron to be 5C. Furthermore, the presence of a low-energy band (<6000 cm^{-1}) with the absence of a feature >10000 cm^{-1} suggests a 4C iron, though a highly distorted 5C site cannot be ruled out based on this alone. As shown below, only a 4C+5C biferrous site (which will be referred to as Fe1 and Fe2, respectively) assignment is consistent with the VTVH MCD data. Thus for DFsc and each variant, the two
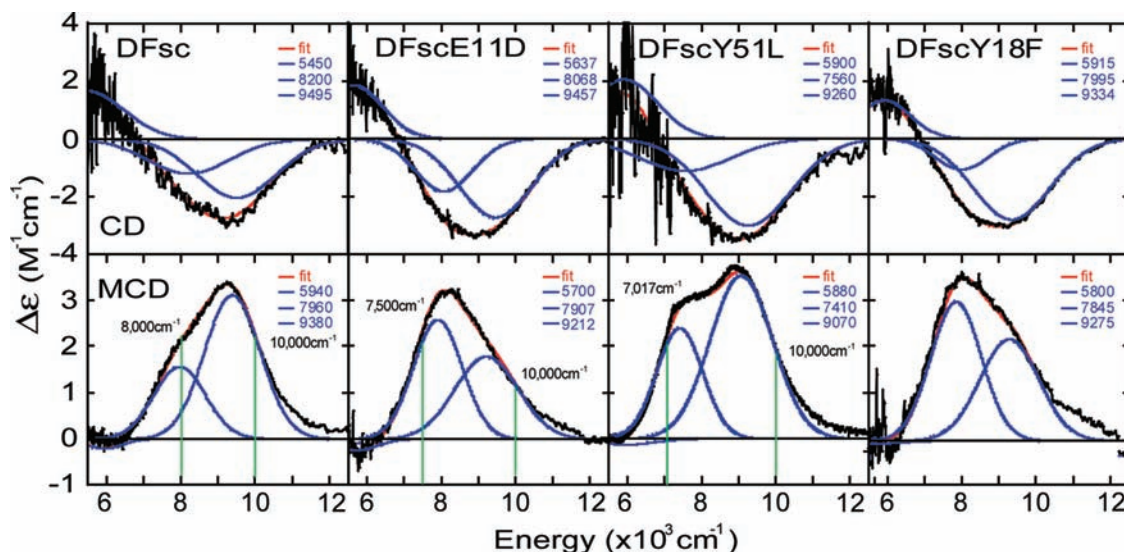
FIGURE 2: CD/MCD spectra of biferrous DFsc, DFscE11D, DFscY51L, and DFscY18F. The top four panels are CD spectra (black) collected at 4 °C for each DFsc peptide overlaid with the simulated spectrum (red) obtained by summing Gaussian transitions (blue). The bottom four panels are MCD spectra (black) collected at 5 K and 7 T (with 0 T data subtracted out to correct for any baseline effects and LT CD signals) with simulated data (red and blue). Vertical green lines in DFsc, DFscE11D, and DFscY51L MCD panels show where VTVH MCD data were collected.

Table 1: Summary of Gaussian Resolution to Biferrous CD/MCD Data for DF Peptides

band	DFsc		DFscE11D		DFscY51L		DFscY18F	
	CD (cm^{-1})	MCD (cm^{-1})	CD (cm^{-1})	MCD (cm^{-1})	CD (cm^{-1})	MCD (cm^{-1})	CD (cm^{-1})	MCD (cm^{-1})
1	5450	5940	5637	5700	5900	5880	5915	5800
2	8200	7960	8068	7907	7560	7410	7995	7845
3	9495	9380	9457	9212	9260	9070	9334	9275

lower energy transitions (band 1 and 2 in Table 1) are assigned as arising from a distorted tetrahedral Fe^{II} center and the highest energy transition (band 3 in Table 1) to a distorted trigonal bipyramidal iron. The observation that Y51 → L perturbation shifts the energy position of the 7960 cm^{-1} band in DFsc by ~550 cm^{-1} while not significantly affecting the highest energy band supports the assignments above and suggests that this residue exerts an influence on the LF of the 4C iron. The lowest energy LF transition has low signal-to-noise ratio precluding reliable detection of possible perturbation.

VTVH MCD. Since the Y51L substitution caused a significant change in the MCD spectrum, relative to DFsc these two peptides were selected for VTVH MCD data collection and analysis. VTVH MCD data were also collected on DFscE11D because this sample was used for oxidized XAS studies due to its increased stability (*49*), but the results are equivalent to those for DFsc and are presented in the Supporting Information.

Normalized VTVH MCD data for biferrous DFsc collected at 10000 and 8000 cm^{-1} (vertical green lines in Figure 2 show the energy positions at which data were collected) and for biferrous DFscY51L collected at 10000 and 7020 cm^{-1} are shown in Figure 3 and Figure S4. These energies were chosen to minimize contributions from the overlap between bands. The observed MCD intensity increases as the temperature is decreased, behavior indicative of MCD *C*-terms associated with paramagnetic doublet ground states that are split in a magnetic field. The saturation magnetization behavior collected on equivalent MCD bands is highly similar for the series, suggesting that the biferrous sites all have similar ground state electronic structures (Figure S3). Interestingly, the isotherms collected at different wavelengths

overlay within standard deviation for DFsc but not DFscY51L (Figure S4). The saturation magnetization curves for DFscY51L collected at 7020 cm^{-1}, the band perturbed by the Y → L variation, are distinctly different from those collected at 10000 cm^{-1}, consistent with the above result that the 9070 and 7410 cm^{-1} LF transitions are from different iron centers.

The VTVH MCD data were first fit using a doublet model (energy level diagram shown in Figure 4), as previously described (*50*). The float parameters in this method are $(A_{sat\ lim})_i$, B_i, δ_i, $g_{i\parallel}$, $g_{i\perp}$, E_i, and M_z/M_{xy} which are the *C*-term and *B*-term MCD intensity, the rhombic ZFS of the *i*th doublet, dimer effective *g*-values of the *i*th doublet, the energy of the *i*th sublevel, and the ratio of the transition dipole moments for the directions indicated, respectively. Initially, the lowest temperature data were fit using only a ground doublet starting with possible $g_\parallel$ values of 4, 8, 12, and 16 and setting $g_\perp = 0 = M_z/M_{xy}$. Once other parameters were optimized, $g_\perp$ and M_z/M_{xy} were allowed to deviate from zero, but no improvement of the fits was observed. A satisfactory fit to each set could only be obtained with GS parameters of $g_\parallel \cong 4$, and $\delta \sim 3.8$ and ~ 5.5 cm^{-1} for DFsc and DFscY51L, respectively. Isotherms were sequentially added to the fit until a single doublet could no longer accurately reproduce the data (this occurred upon inclusion of the third, 5 K, isotherm) and an additional excited state (both singlet and doublet) was included in the model with the GS doublet parameters fixed. In order to fit the complete data sets (up to 25 K), an excited state doublet with $g_\parallel \cong 8$ (i.e., $M_s = \pm2$) at ~3.5 and ~6.0 cm^{-1} was required for the DFsc and DFscY51L VTVH MCD data sets, respectively. The values shown in the insets of Figure 3 give the best fits
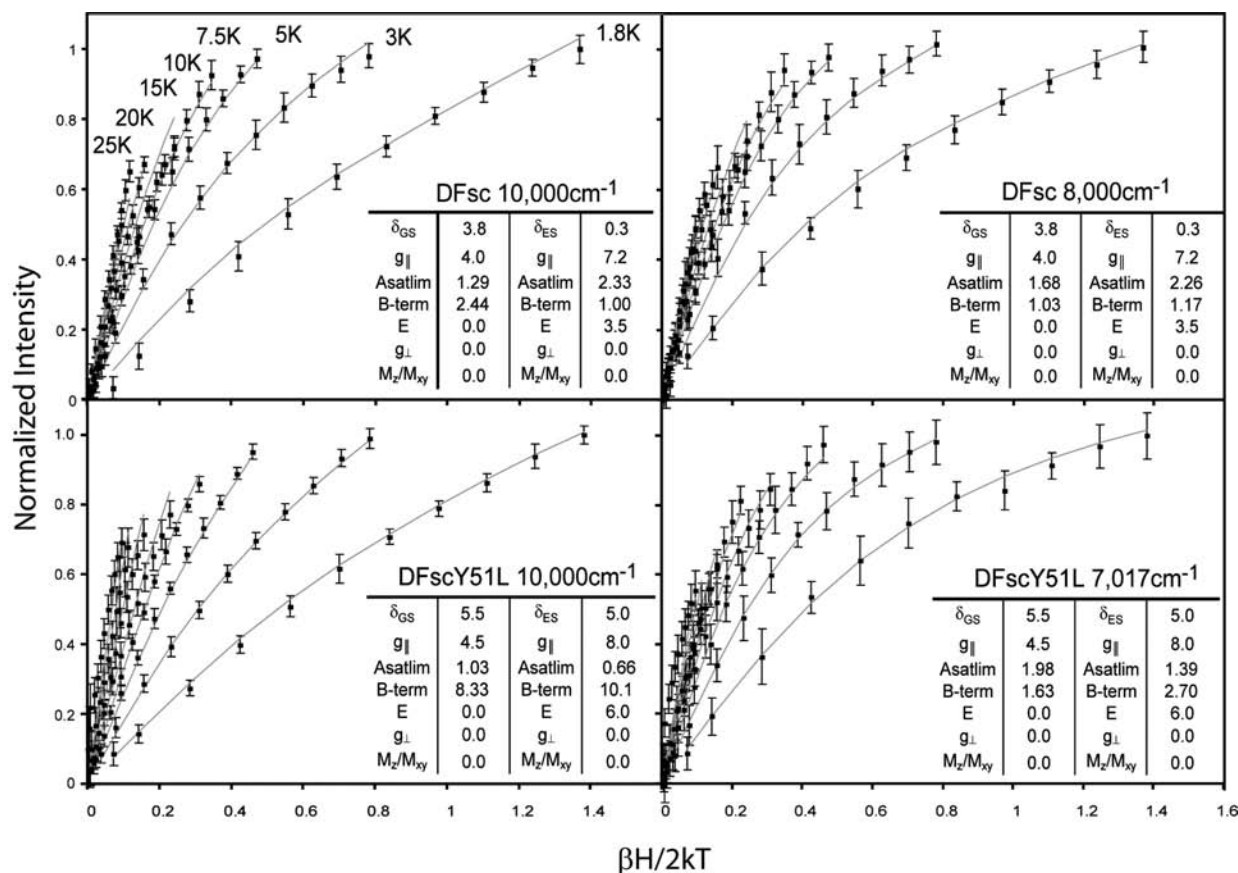
FIGURE 3: VTVH MCD data of biferrous DFsc and DFscY51L. Normalized data collected at the energies indicated in each panel are represented by points with standard deviation in black. Temperatures at which each isotherm was collected are shown in the top left panel. Data were simulated using the doublet model, as described in the text, and are overlaid as gray lines; the parameters extracted from analysis are summarized in each inset.

to the data; however, in Table 2 ranges that are still permissible within the error of the data are reported. Inclusion of a second ES did not significantly improve the fits. The final best fits, as reported in the insets of Figure 3 and Figure S5, were obtained by relaxing all constraints and allowing the parameters to float from the previously optimized values. From this analysis the electronic description of the ground and excited states as well as the energy of the ES are very similar (Table 2). The experimentally observed difference

FIGURE 4: Energy level diagram for doublet model used to simulate biferrous VTVH MCD data. E is the energy spacing between the ground and excited states (GS and ES), g_{GS} and g_{ES} are the g-values for the ground and excited states, respectively, and δ is the rhombic ZFS parameter.

between the 10000 and 7020 cm^{-1} data sets of DFscY51L is due to variations in the $A_{\text{sat lim}}$ and B-term values for the ground and excited doublets for the two data sets. As shown below, this reflects that each LF transition is associated with a different Fe^{II}.

These doublets reflect the energy levels of a binuclear iron site (Figure 5). If a ferrous site deviates from O_h or T_d symmetry, the $S = 2$ non-Kramers ion splits due to axial (D_i) and rhombic (E_i) ZFS. Additionally, exchange (J), mediated by bridging ligands, will couple the two $S = 2$ ions to give $S_{\text{tot}} = 4, 3, 2, 1$, and 0 dimer states which also split in energy. Since the exchange and ZFS terms are comparable in magnitude for binuclear non-heme ferrous systems, they need to be simultaneously considered using the spin Hamiltonian:

$$H = -2J\mathbf{S}_1 \cdot \mathbf{S}_2 + D_1\left(\mathbf{S}_{z_1}^2 - \frac{1}{3}S(S+1)\right) + E_1(\mathbf{S}_{x_1}^2 - \mathbf{S}_{y_1}^2) + D_2$$
$$\left(\mathbf{S}_{z_2}^2 - \frac{1}{3}S(S+1)\right) + E_2(\mathbf{S}_{x_2}^2 - \mathbf{S}_{y_2}^2)$$

where J is the exchange coupling between the two irons (negative values reflect antiferromagnetic exchange) and D_i and E_i are the axial and rhombic ZFS parameters for each ferrous center. Diagonalization of the matrix associated with this Hamiltonian gives the wavefunctions of biferrous spin systems and their energies. Various combinations of the exchange and ZFS parameters produce correlation (i.e., J/D) diagrams with specific GS properties. (Many situations are summarized in ref 1.) From the doublet model analysis
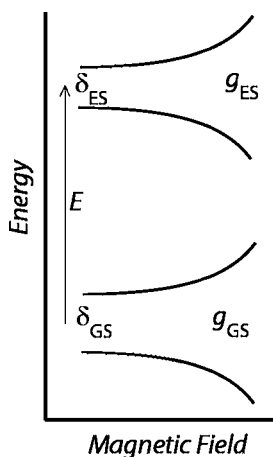
Table 2: Summary of Physical Parameters Derived from Fits to the Biferrous DF Peptide VTVH MCD Data[a]

parameter	DFsc		DFscE11D		DFscY51L	
	10000 cm^{-1}	8000 cm^{-1}	10000 cm^{-1}	7500 cm^{-1}	10000 cm^{-1}	7020 cm^{-1}
δ_{GS} (cm^{-1})	3.8	3.8	4.9	4.9	5.5	5.5
$g_{GS\parallel}$	4.0	4.0	4.0	4.0	4.5	4.5
$A_{sat\ lim}$	1.29	1.68	2.03	2.3	1.03	1.98
B-term	2.44	1.03	1.13	0.03	8.33	1.63
δ_{ES} (cm^{-1})	0.3	0.3	2.0	2.0	5.0	5.0
$g_{ES\parallel}$	7.2	7.2	8.7	8.749	8.0	8.0
$A_{sat\ lim}$	2.33	2.26	1.77	2.15	0.66	1.39
B-term	1.00	1.14	2.94	1.46	10.1	2.70
E_{ES} (cm^{-1})[b]	1 to 5	3 to 7	3 to 7	4 to 8	4 to 8	3 to 8
J (cm^{-1})[b]	−2.9 to −1.5	−2.1 to −1.0	−1.1 to −0.7	−1.3 to −0.8	−1.1 to −1.9	−2.6 to −1.0
D_1 (cm^{-1})[b]	−4 to −5[c]	8 to 10[c]	−4 to −5[c]	7 to 8[c]	−3 to −5	6 to 11
E/D_1[b]	∼0.33[c]	<0.08[c]	∼0.33[c]	<0.08[c]	∼0.33	<0.15
D_2 (cm^{-1})[b]	9 to 10[c]	−4 to −5[c]	8 to 9[c]	−4 to −5[c]	6 to 8	−4 to −6
E/D_2[b]	<0.08[c]	∼0.33[c]	<0.08[c]	∼0.33[c]	<0.08	∼0.33

[a] Columns summarize parameters from both fitting methods described in the text for the DF variant and wavelength specified. [b] The ranges given were determined by systematically perturbing from the best fit value (given in insets of Figure 2) until the simulated saturation behavior was no longer within the error bars of the data sets. [c] For these values the subscripts (i.e., D_1 to D_2) can be interchanged and still reproduce the data.
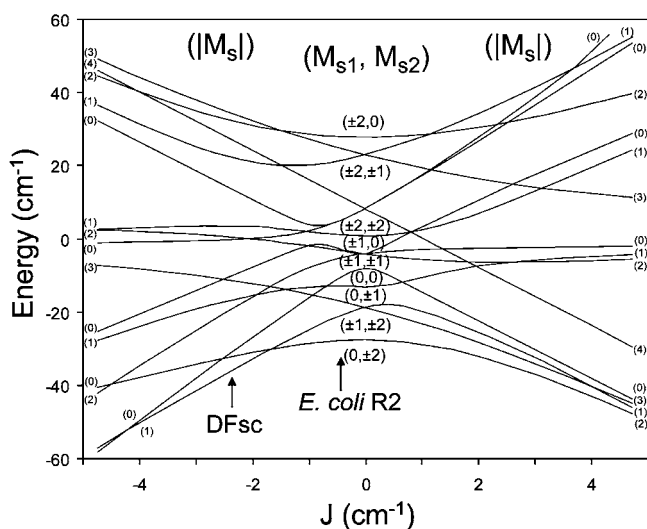

FIGURE 5: Correlation (J/D) diagram of the energy levels of the biferrous system including exchange coupling and single-site ZFS. The exchange coupling (J) is varied from −5 to +5 cm^{-1}. The central portion gives the pure ZFS limit with states labeled with M_S values for each uncoupled Fe^{II} (M_{S1}, M_{S2}). The right side indicates a ferromagnetic interaction ($J > 0$) between the ferrous atoms and the left an antiferromagnetic interaction ($J < 0$) The spin Hamiltonian used for generating the diagram is shown in the text, with $D_1 = -4.9$ cm^{-1}, $D_2 = +9.0$ cm^{-1}, and $E_1 = E_2 = 0$, the GS D values for DFsc determined by fits using the spin Hamiltonian analysis to the 10000 cm^{-1} data set (see Figure 6, top left). Note that *E. coli* R2 has been added for comparison; however, the actual D values differ from those used to make this diagram.

above, all of the DFsc peptides have $g_{GS\parallel} \cong 4$ and $g_{ES\parallel} \cong 8$. This indicates the GS is $M_s = \pm 1$ and the first ES is $M_s = \pm 2$. This GS electronic structure can only arise in magnetically coupled ferrous dimer systems when the axial ZFS parameters (D) are of opposite signs and the exchange coupling (J) is weakly antiferromagnetic (1). A representative J/D diagram describing this situation is shown in Figure 5, with $D_1 = -4.9$ cm^{-1}, $D_2 = +9.0$ cm^{-1}, and $E_1 = E_2 = 0$. In this diagram, the $M_s = \pm 1$ GS and $M_s = \pm 2$ ES configuration is only observed over the range of $J \approx -1.4$ to −2.7 cm^{-1} (note that the spin crossover point is a function of both D_1 and D_2). Inclusion of the rhombic terms or noncollinear ZFS tensors in the J/D diagram removes all degeneracy and produces mixed wave functions; however,

the relative energy ordering of the spin states is not significantly affected (1). From LF theory, 6C sites can have either positive or negative D values describing a compression or elongation along a unique axis, respectively. Square pyramidal (5C) and trigonal bipyramidal (5C) sites are typically observed with −D values, while T_d sites found in proteins are almost exclusively flattened and thus described by a +D. Since 6C iron is ruled out by the MCD spectra (Figure 2), the site geometry can be assigned by the signs of the D's as 4C+5C.

Quantitative descriptions of the biferrous sites' ground state electronic structure were obtained by fitting the VTVH MCD data directly to this spin Hamiltonian (52). From the above results, the exchange coupling was constrained to 0 < −J < 4 cm^{-1}, and the individual Fe^{II} centers were required to have oppositely signed D values (constrained to <|15 cm^{-1}|, the maximum value observed in model studies). Figure 6 shows simulations obtained for the VTVH MCD data for DFsc and DFscY51L. (Figure S6 shows the best fit simulations obtained for the DFsc, DFscE11D, and DFscY51L VTVH MCD data sets.) MCD intensity is proportional to the spin-expectation values of the single iron center being probed projected onto the dimer states (i.e., the iron responsible for the transition on which the data are collected, and given the subscript 1 for ZFS parameters in this analysis). For DFsc satisfactory simulations can obtained with both $D_1 > 0/D_2 < 0$ or $D_1 < 0/D_2 > 0$ (see Figure S6, panels A−D), and therefore correlating D_i's with specific MCD transitions cannot be made from this alone. There is, however, a preference for assigning the −D to the higher energy band since the best fit in the alternative situation no longer has a $M_s = \pm 1$ GS (Figure S6, panel C). For all fits the iron with a −D required an E/D of ∼0.33 and the iron with the +D an E/D < 0.08. The GS electronic structure descriptions obtained by directly fitting to the spin Hamiltonian are analogous to those from the dimer model (i.e., the M_S of the ground and excited spin states, δ_{GS}, and energy of the first ES) giving confidence to the fits. The parameters extracted for the best fits to each data set are given in the insets of Figure 6 and Figure S6, and the range of values that can still reproduce the data within error are summarized in the bottom portion of Table 2. The ground state electronic structure of DFsc is best described as a weakly antiferro-
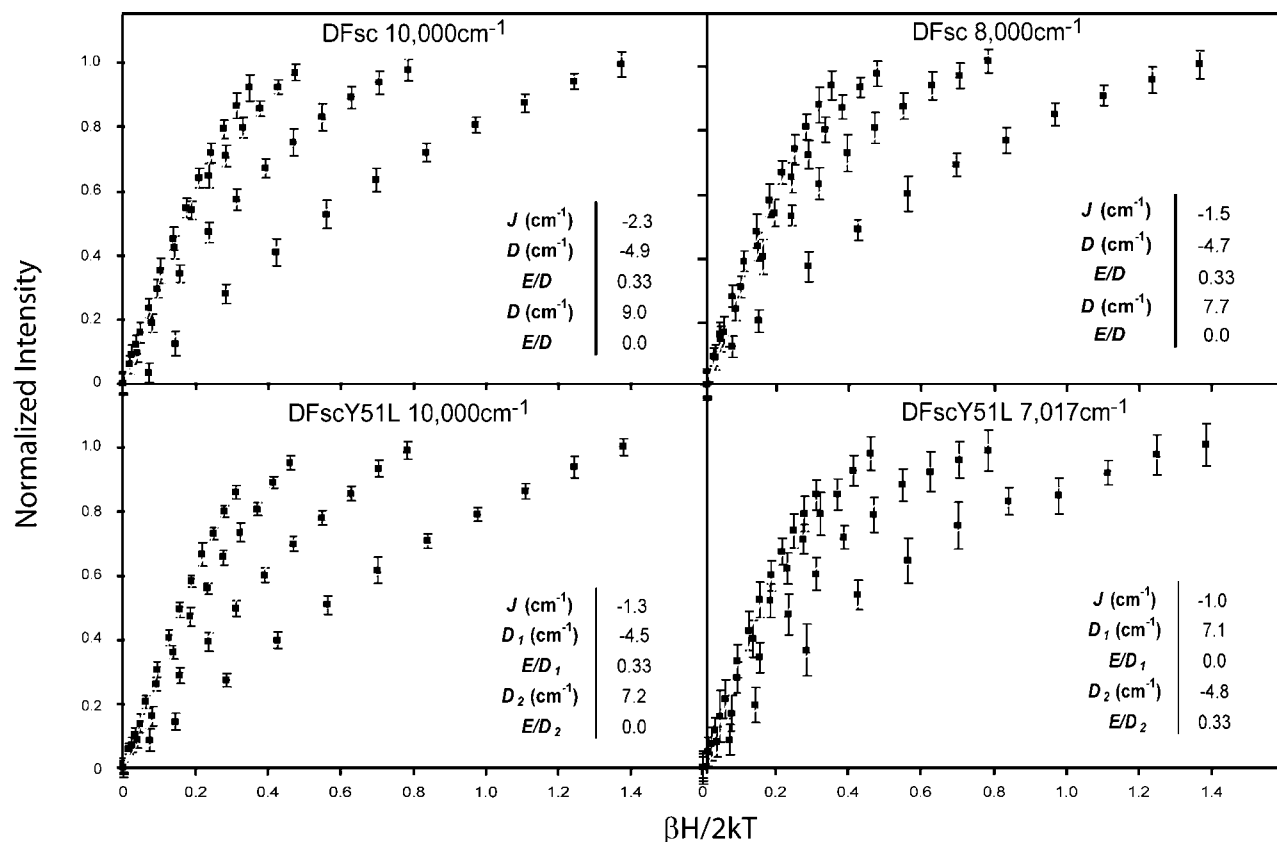
FIGURE 6: Biferrous VTVH MCD data of DFsc and DFscY51L overlaid with simulations using the binuclear Hamiltonian. Each panel shows the four lowest temperature isotherms (data points) collected on the variant and energy described in each panel. Solid lines show the best fits to the complete data sets (i.e., all isotherms up to 25 K) from spin Hamiltonian analysis described in the text to the data, and extracted parameters are shown in insets. The values reported in the insets correspond to the best fit shown; however, Table 2 gives values for each physical parameter based on other fits to the data that are still within the experimental error of the data.

magnetically coupled ($-2.9 > J > -1.0$ cm^{-1}) biferrous system with D values of $-5 > D > -4$ cm^{-1} and $10 > D > 8$ cm^{-1}.

Unlike the VTVH MCD data collected for DFsc, the two data sets collected at 10000 cm^{-1} and 7020 cm^{-1} for DFscY51L do not overlay within standard deviation and allow firm assignments of ZFS parameters to specific Fe^{II} centers. The bottom two panels of Figure 6 and the panels I though L of Figure S6 show the best fits obtained for the DFscY51L VTVH MCD data using the spin Hamiltonian analysis. In Figure S6, panels I and K show the fits to the VTVH MCD data collected at 10000 cm^{-1}, on the band assigned to the 5C Fe^{II}, *vide supra*. The $D_1 > 0/D_2 < 0$ fit does not accurately reproduce the data (Figure S6, panel K). However, the $D_1 < 0/D_2 > 0$ fit (bottom left panel of Figure 6 and panel I of Figure S6) does and gives the same electronic description obtained from the doublet fit (bottom left panel of Figure 5). The J, D_1, and D_2 obtained are -1.3, -4.2, and $+7.2$ cm^{-1}, respectively (values quoted are from the best fit to the 10000 cm^{-1} data set, since the signal-to-noise ratio is considerably higher; ranges are given in Table 2). Again, the iron with a $-D$ is best described by an E/D of 0.33 and the $+D$ iron by an E/D of $< \sim 0.08$. The VTVH MCD data collected at 7020 cm^{-1} (note, the standard deviation on this data set is larger due to its decreased intensity and lower energy) can be simulated, within standard deviation, with either $D_1 > 0/D_2 < 0$ (bottom right panel of Figure 6 and panel J of Figure S6) or $D_1 < 0/D_2 > 0$ (panel L in Figure S6). However, the $D_1 > 0/D_2 < 0$ fit (bottom

right panel of Figure 6 and panel J of Figure S6) is visually better and agrees with the parameters extracted from the VTVH MCD data from the 10000 cm^{-1} band (Table 2). From this analysis, the 7410 cm^{-1} MCD transition in DFscY51L is associated with a positive D value of $\sim$7.2 cm^{-1} and E/D ratio close to zero (Fe1) and the 9070 cm^{-1} transition with a negative D value of approximately -4.5 cm^{-1} and an E/D of 0.33 (Fe2). From Table 2, the largest effect of the Y51 → L perturbation is a slight lowering of the $+D$ value relative to DFsc. This also suggests that Y51 exerts a dominant effect on the LF of Fe1 consistent with the above MCD results. The site geometry and band assignments of DFsc and DFscE11D, both 4C+5C, are made by correlation to the results for DFscY51L and the fact that the E11D and Y51L variations do not significantly affect the first shell as observed in EXAFS spectra of the biferrous peptides (*vide infra*).

UV/Vis Absorption Spectroscopy. The biferrous sites of DFsc and its amino acid variants react rapidly with O_2. The spectroscopically observable species formed in the reactions are shown in Figure 7. The apparent formation rate constants for DFsc and DFscE11D have been previously reported as 2.1 ± 0.1 and 4.4 ± 0.3 s^{-1}, respectively (*49*). A similar analysis for the tyrosine mutants gives apparent formation rate constants of 5.1 ± 0.7 and 2.3 ± 0.2 s^{-1} for DFscY51L and DFscY18F, respectively (Figure S8). In DFsc, DFscE11D, and DFscY18F, the species formed have a λ_{max} at $\sim$520 nm with molar extinction coefficients (ϵ) of $\sim$1500 to 2000 mM^{-1} cm^{-1}. The 520 nm feature has previously been
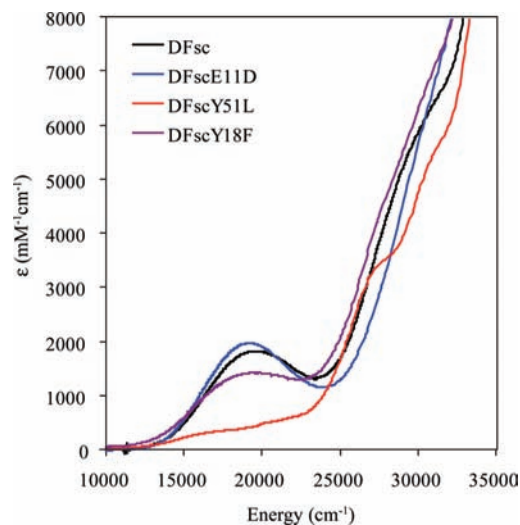
FIGURE 7: UV/vis absorption spectra of species formed upon reaction of DF variants with O_2. Peptide concentration was 100 μM anaerobically incubated with 200 μM ferrous iron prior to reaction with an equal volume of O_2 saturated buffer. Spectra were collected allowing the reaction to progress 2 s for DFsc and 1 s for all other variants.

FIGURE 8: Fe K-edge spectra for biferrous DFsc, biferrous DFscY51L, biferrous DFscE11D, and oxidized (biferric) DFscE11D. The inset shows the magnified pre-edge region.

assigned, using resonance Raman spectroscopy, for DFsc and DFscE11D as a phenolate to ferric charge transfer transition (*49*). Two pseudosymmetric Y residues are present in the DFsc protein at ~4 Å from each of the two iron atoms approximately collinear with the Fe−Fe vector (based on diZn NMR structure) (*47*). Thus either could bind terminally to one ferric center of the binuclear site. Removal of Y18 does not result in the loss of the 520 nm feature, while removal Y51 does (Figure 7). This indicates that Y51 is coordinated to iron in the biferric state and the source of the 520 nm charge transfer transition. The 520 nm species has previously been shown to be significantly more stable in DFscE11D relative to DFsc, and thus this variant was selected for the oxidized XAS studies below (*49*).

XAS Spectroscopy. (A) Fe K Edge of Biferrous Sites. Figure 8 shows a comparison of the iron K-edge X-ray absorption spectra for DFsc, DFscY51L, and DFscE11D, where the XAS data for each peptide correspond to an average over the binuclear site. The rising edge energy position is consistent with the Fe^{II} oxidation state and is similar for the three peptides, suggesting similar effective nuclear charges. Because the shape and intensity of the metal K-edge region are sensitive to both near- and long-range structure at the metal site, the observation that the edge spectra do not completely coincide in the 7110−7150 eV region indicates that some minor differences exist in the local structure of the iron centers, as observed in MCD, *vide supra*. In particular, the edge shape and intensity are more similar between DFsc and DFscY51L than between DFsc and DFscE11D, suggesting that the Y51L mutation perturbs the local structure of the iron cluster of DFsc to a lesser extent than does E11D. This result serves as indirect evidence that Y51 is not directly bound to the iron in biferrous DFsc.

The iron K-pre-edge shape and intensity pattern in the 7108−7116 eV energy region are probes of oxidation and spin state, coordination number, and geometry at the average iron site (*55*). The total pre-edge area typically increases with a decrease in the centrosymmetry of the iron site through increased iron 3d-4p mixing, such that 6C high-spin mono-
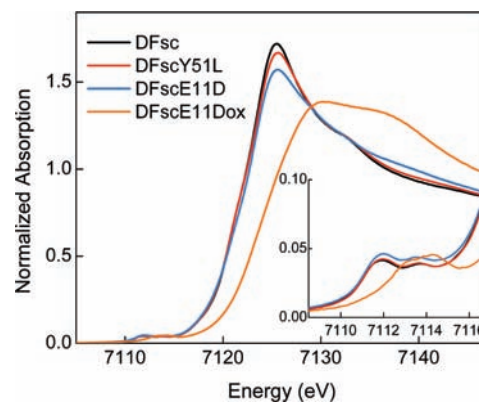
nuclear ferrous complexes have a pre-edge intensity of ~4 units, while 5C and T_d mononuclear models are typically fit with ~12 and ~15 units of intensity, respectively. The pre-edge spectra of DFsc, DFscY51L, and DFcsE11D consist of two peaks centered at 7111.8 and 7113.7 eV with the total pre-edge area of 8.3−9.4 units (Figure 8, inset; Table 3). The number and energy position of these peaks are characteristic of high-spin ferrous species, but the integrated intensity falls into a region intermediate between 6C and 5C/4C complexes. However, the MCD results rule out the possibility of 6C iron for any of the DFsc peptides. Hence, the pre-edge intensity and, consequently, 3d-4p mixing are somewhat lower for the DFsc peptides than for mononuclear 4C and 5C model compounds.

(B) EXAFS of Biferrous Sites. The iron K-edge k^3-weighted EXAFS data, corresponding Fourier transforms (FT's), and representative multishell EXAFS fits for DFsc, DFscY51L, and DFscE11D are displayed in Figure 9a,b. The results of the EXAFS curve-fitting analysis of the first iron coordination sphere and visual representation of the respective fits are given in Table 4 and Figure S7 (a−i). In addition to first sphere O/N atoms, each fit in Table 4 includes a shell of carbon scatterers at ~3.0 Å, typically required in fits to EXAFS data of many non-heme binuclear iron enzymes as carbon atoms of ligating carboxylates and imidazoles. Inclusion of this shell visual improves the fit to the first shell in R'-space, and a coordination number of 2 gives the lowest fit error value.

For DFsc, a single first shell composed of 4, 5, or 6 O/N scatterers leads to an incomplete fit to the first-shell peak (Table 4, fit 1, and Figure S7 (a)), and hence a split first shell of 2 and 3 O/N atoms at 2.03 and 2.16 Å, respectively,

Table 3: XAS Pre-edge Fit Results for Biferrous DFsc, Biferrous DFscY51L, Biferrous DFscE11D, and Oxidized DFscE11D

sample	pre-edge peak energy	pre-edge peak intensity[a]	total pre-edge peak intensity[a]
DFsc	7111.79 (0.04)	5.8 (0.7)	8.3 (0.7)
	7113.68 (0.07)	2.5 (0.6)	
DFscY51L	7111.80 (0.02)	5.8 (0.5)	9.4 (0.6)
	7113.66 (0.05)	3.6 (0.5)	
DFscE11D	7111.84 (0.03)	6.1 (0.7)	9.1 (0.6)
	7113.65 (0.08)	3.0 (0.3)	
oxDFscE11D	7113.36 (0.07)	8.6 (1.5)	9.6 (1.4)
	7114.59 (0.04)	1.0 (0.2)	

[a] Values reported for the pre-edge intensity are multiplied by 100 for convenience.
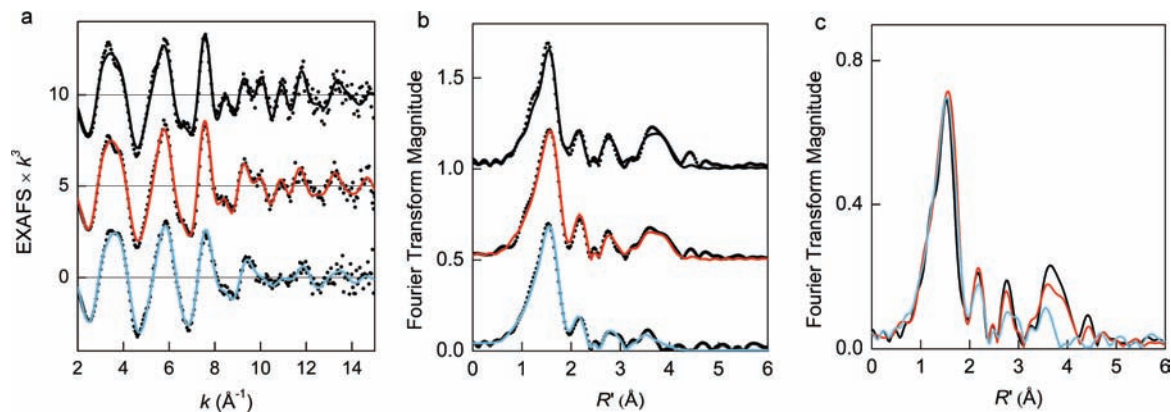
FIGURE 9: (a) Fe K-edge EXAFS and (b) non-phase-shift corrected Fourier transforms of biferrous (top to bottom) DFsc, DFscY51L, and DFscE11D. Experimental data, dots; representative multishell fits from Table 5, solid lines. (c) Non-phase-shift corrected Fourier transforms of experimental EXAFS data for biferrous DFsc (black), DFscY51L (red), and DFscE11D (blue).

Table 4: First-Shell EXAFS Curve-Fitting Results for Biferrous DFsc, Biferrous DFscY51L, and Biferrous DFscE11D[a]

		DFsc at fit no.			DFscY51L at fit no.			DFscE11D at fit no.		
		1	2	3	4	5	6	7	8	9
Fe−O/N[b]	N	5	2	2	5	2	2	5	2	2
	R (Å)	2.07	2.02	2.03	2.07	2.02	2.03	2.07	2.01	2.02
	$\sigma^2 \times 10^5$ (Å^2)	1230	370	390	1040	470	530	1140	500	540
Fe−O/N[b]	N		3	3		3	3		3	3
	R (Å)		2.16	2.16		2.14	2.14		2.13	2.14
	$\sigma^2 \times 10^5$ (Å^2)		650	700		670	810		710	820
Fe−C	N			1			1			1
	R (Å)			2.55			2.55			2.54
	$\sigma^2 \times 10^5$ (Å^2)			470			200			400
Fe−C	N	2	2	2	2	2	2	2	2	2
	R (Å)	2.96	3.00	3.00	2.96	2.99	2.99	2.96	3.01	3.01
	$\sigma^2 \times 10^5$ (Å^2)	590	390	430	730	460	570	1000	760	810
ΔE_0 (eV)		−9.1	−6.0	−5.7	−8.4	−6.0	−5.9	−7.1	−4.6	−4.4
F^c		0.433	0.393	0.391	0.345	0.333	0.309	0.270	0.255	0.233

[a] All fits were performed over the k range of 2−15 Å^{-1}. The estimated uncertainty in R is ±0.02 Å for the first shell and ±0.05 Å for outer shells; the uncertainty in N is ∼25%. [b] Scatterers differing by $Z \pm 1$ are not distinguishable in an EXAFS fit. The first element in a pair indicates the type of atom used to model the backscattered wave in the FEFF calculation. [c] The goodness of the fit is defined as $F = [\Sigma(k^6(\chi_{exptl} - \chi_{calcd})^2)/(\Sigma k^6\chi_{exptl}^2)]^{1/2}$.

is used to model the data (fit 2 and Figure S7 (b)). It should be noted that the difference in these bond lengths is close to the resolution limit of the current data (0.11 Å). In contrast, the data for DFscY51L and DFscE11D are well fit with a single shell of 5 O/N scatterers at 2.07 Å (fits 4 and 7, Figure S7 (d, g)), which suggests that individual Fe−ligand distances have a higher static disorder than for DFsc and thus may be combined into a single shell. A very high Debye−Waller factor of ∼0.01 Å^2 for a single shell in all samples indicates that there is a wide range of Fe−O/N distances for the two iron atoms. If a split first-shell model is used for all peptides (fits 2, 5, and 8), on going from DFsc to DFscY51L to DFscE11D both short and long-distance Fe−O/N interactions remain at approximately the same distance of 2.02−2.01 and 2.16−2.13 Å, while the corresponding σ^2 values increase for the two variants. These results imply that Y51L and E11D replacements only slightly perturb the iron−ligand distances in the first shell of DFsc.

Interestingly, for all DFsc peptides, a three-component fit to 3.0 Å, such as fit 2, does not properly model the intensity of the small peak in the FT centered at ∼2.2 Å (Figure S7 (b, e, h)), even if additional outer-shell scattering components are added to the fit to account for the scattering up to 5.0 Å. A visual improvement to this peak is achieved when a light atom is included at ∼2.55 Å (fits 3, 6, and 9 and Figure S7 (c, f, i)), modeled as the carbon of a bidentate carboxylate.

Reducing the coordination number from 1.0 to 0.5 leads to a negative σ^2 value for this component; however, determination of the exact coordination number is complicated by the fact that the scattering amplitude of a single light atom at 2.5 Å is low and highly correlated to N and σ^2 of surrounding O/N and C shells.

While the iron environment up to R' of ∼2.4 Å is extremely similar for the three samples, the outer-sphere scattering for 2.4 < R' < 4.0 Å reveals structural differences between the DFsc peptides (Figure 9c). Particularly, the amplitude of the FT peaks at R' ∼2.8 and ∼3.8 Å in the spectrum of DFsc is substantially reduced for DFscE11D. Detailed fits to the outer-shell region have been performed to establish whether the observed differences can be related to changes in the Fe−Fe separation within the cluster (see Supporting Information). For DFsc, starting with fit 3 in Table 4, an Fe atom can be included at 3.3 Å with σ^2 of 0.0150 Å^2 or at 4.1 Å with σ^2 of 0.0043 Å^2. The former contribution has a very large σ^2 value, and therefore such fits are discarded, while the inclusion of the latter component models the broad peak between 3.0 and 4.0 Å in the FT incompletely (Figure S8, fit d2). To match the observed FT pattern, a number of additional single and multiple scattering paths are necessary; however, the Fe−Fe component in the final fit can be substituted with a shell of five carbon atoms at a similar distance with an equivalent goodness-of-fit value

(Table S1 and Figure S8, fit d6 vs d5). This result indicates that for DFsc it is not be possible to discriminate between a potential Fe—Fe component at ∼4 Å and light atom scatterers at a similar distance originating from protein-derived ligands. This previously described limitation of the EXAFS analysis of binuclear metal proteins with unknown spatial structure is due to a high degree of correlation between metal—metal and metal—carbon waves at long distances and the low intensity of the Fe—Fe scattering wave in diiron clusters with a long Fe—Fe separation and no rigid bridging ligands such as oxo or multiple hydroxo ligands (*58*). With either Fe—Fe or Fe—C components contributing to the peak at ∼3.8 Å of FT for DFsc, the need for additional scattering components indicates that imidazolyl and carboxylate groups contribute measurably to outer-shell scattering. In addition, the pattern and intensity of the FT features for DFsc are comparable to those for $Fe_2(\mu\text{-}O_2CAr^{Tol})_4(t\text{-}Bu\text{-}Py)_2$, a biferrous complex with four carboxylato bridges whose outer-shell peaks between 2.4 Å < R' < 4.0 Å arise solely from single and multiple scattering from light atoms of the pyridine and carboxylate groups (Figure S9). Taken together, these results suggest that the outer shells for DFsc are dominated by the contributions from the imidazolyl ring and carboxylate groups and can be reasonably modeled without an Fe—Fe component.

For DFscE11D, the multishell EXAFS fit using the same components as for DFsc for direct comparison results in reduced coordination numbers and large σ^2 values for the outer shells relative to those of DFsc (Table 5). Alternative fits with the Fe—Fe contribution to the distant FT peak display the same fit quality and again low coordination numbers and high σ^2 values for outer-shell components; the putative Fe—Fe distance remains at the same value as for DFsc within the error of the EXAFS analysis (Table S1). For DFscE11D, both structural models are consistent with the disruption of the coherence of single- and multiple-scattering paths originally present in DFsc data, possibly by affecting the spatial orientation of the carboxylate from the mutated residue or by changing the Fe—ligand distances at the same iron. In contrast, the Y51L substitution leaves the outer shells of DFsc mostly intact (Figure 9c and Table 5), thus suggesting that Y51L is not directly bound to the Fe in DFsc.

(C) Fe K Edge of Oxidized DFscE11D. The iron X-ray absorption K-edge shifts to higher energy from reduced to oxidized DFscE11D (Figure 8, orange), with the magnitude of the shift consistent with conversion from a biferrous to a biferric site. The fit to the pre-edge area (Figure 8, inset) requires two peaks centered at 7113.4 and 7114.6 eV, with areas of 8.6 and 1.0 units, respectively (Table 3). These pre-edge features fall within the energy range of high-spin ferric compounds (*55*), further supporting the oxidation state assignment from the edge shift. Oxidation of both Fe's is supported by the result that no substantial absorption intensity is present between 7111.1 and 7111.9 eV, where a lower energy pre-edge peak is observed for model ferrous compounds (*55*) and the biferrous DF peptides (Table 3). The intensity distribution between the two peaks is very different from that observed for μ-oxo bridged biferric model complexes, which typically have an intense higher energy peak of 8−13 units and a lower energy shoulder of 3−4 units (*55*). Therefore, a μ-oxo bridge can be ruled out for oxidized

Table 5: Multishell EXAFS Curve-Fitting Results for Biferrous DFsc, DFscY51L, and DFscE11D[a]

sample		R (Å)	$\sigma^2 \times 10^5$ (Å^2)	ΔE_0	F^c
DFsc	2 Fe—O/N[b]	2.03	380	−5.9	0.241
	3 Fe—O/N	2.16	690		
	1 Fe—C/O	2.55	470		
	2 Fe—C	3.00	430		
	4 Fe—N—C[d]	3.20	430[e]		
	2 Fe—C	3.60	320		
	2 Fe—C	3.78	440		
	5 Fe—C	4.15	560		
	10 Fe—N/C—C/N/O[f]	4.35	560[e]		
DFscY51L	2 Fe—O/N	2.03	530	−6.2	0.191
	3 Fe—O/N	2.13	810		
	1 Fe—C/O	2.55	190		
	2 Fe—C	3.00	670		
	4 Fe—N—C[f]	3.30	670[e]		
	2 Fe—C	3.61	430		
	2 Fe—C	3.78	410		
	5 Fe—C	4.17	670		
	10 Fe—N/C—C/N/O[f]	4.35	670[e]		
DFscE11D	2 Fe—O/N	2.00	530	−4.8	0.194
	3 Fe—O/N	2.13	790		
	1 Fe—C/O	2.54	380		
	2 Fe—C	3.02	780		
	4 Fe—N—C[d]	3.31	780[e]		
	2 Fe—C	3.63	470		
	2 Fe—C	3.79	710		
	3 Fe—C	4.05	1130		
	6 Fe—N/C—C/N/O[f]	4.36	1130[e]		

[a] All fits were performed over the k range of 2−15 Å^{-1}. The estimated uncertainty in R is ±0.02 Å for the first shell and ±0.05 Å for outer shells; the uncertainty in N is ∼25%. [b] Scatterers differing by $Z \pm 1$ are not distinguishable in an EXAFS fit. The first element in a pair indicates the type of atom used to model the backscattered wave in the FEFF calculation. [c] The goodness of the fit is defined as $F = [\sum(k^6(\chi_{exptl} - \chi_{calcd})^2)/(\sum k^6 \chi_{exptl}^2)]^{1/2}$. [d] Modeled as the Fe—N—C path of 128° of an imidazole ring. [e] The σ^2 values for multiple-scattering paths were restricted to those of the corresponding single-scattering paths. [f] Modeled as the Fe—N—C path of 158° of an imidazole ring.

DFscE11D. Diiron complexes with weaker coupling between the iron centers are known to exhibit pre-edge areas consistent with the mononuclear complexes of the same coordination number (*55*). The total pre-edge area of 9.6 units for oxidized DFscE11D is between the areas for 6C (4.0−7.3 units) and 5C (14.4 units) mononuclear high-spin ferric complexes (*55*). It is also higher than the area of 6C biferric complexes containing μ-hydroxo or μ-phenolato bridges (5.5−8.5 units) (*55*). This suggests coordination models for oxidized DFscE11D of either a distorted 6C+6C or a 5C+6C, both lacking an oxo bridge. However, the variable temperature MCD results show that the biferric site in DFscE11D is diamagnetic and therefore antiferromagnetically coupled by some bridging ligand(s) (*49*).

(D) EXAFS of Oxidized DFscE11D. The iron K-edge k^3-weighted EXAFS data and corresponding FT for oxidized DFscE11D are presented in Figure 10. Table 6 shows results of the EXAFS fits using a single first-shell (fits 10−11) and multiple-shell (fits 12−14) models. The best fit to the EXAFS data (Table 6, fit 12, and Figure 10) yields five O/N ligands at an average distance of 2.02 Å, a contraction by 0.05 Å from the first-shell distance for biferrous DFscE11D, consistent with oxidation to a biferric site. The error for a 6C first-shell fit is only slightly higher (Table 6, fit 13, $F = 0.239$ vs 0.232); thus both 5C and 6C models are consistent with the EXAFS data. As for the biferrous precursor, the Debye—Waller factor of 0.01 Å^2 for oxidized DFscE11D suggests that there is a wide range of distances for the first
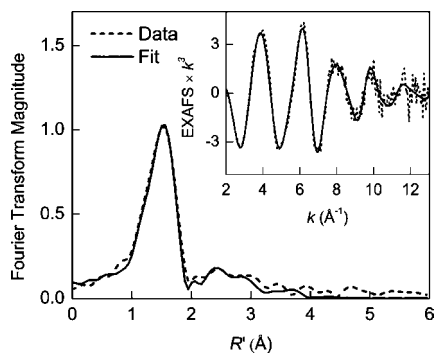
FIGURE 10: Non-phase-shift corrected Fourier transform and Fe K-edge EXAFS data (inset) for oxidized (biferric) DFscE11D. Data (dashed line); fit 12 (solid line).

Table 6: EXAFS Curve-Fitting Results for Oxidized DFscE11D[a]

fit no.		R (Å)	$\sigma^2 \times 10^5$ (Å^2)	ΔE_0	F^b
10	5 O/N	2.02	970	−4.3	0.308
11	6 O/N	2.02	1170	−4.5	0.315
12	5 Fe−O/N[c]	2.02	960	−4.4	0.232
	2 Fe−C	2.97	530		
	2 Fe−C	3.34	720		
	4 Fe−N−C/N[d]	4.18	740		
13	6 Fe−O/N[c]	2.02	1160	−4.8	0.239
	2 Fe−C	2.97	530		
	2 Fe−C	3.33	740		
	4 Fe−N−C/N[d]	4.17	650		
14	0.5 Fe−O	1.89	450	−5.0	0.226
	5 Fe−O/N	2.03	870		
	2 Fe−C	2.97	550		
	2 Fe−C	3.33	750		
	4 Fe−N−C/N[d]	4.17	640		

[a] All fits were performed over the k range of 2−13 Å^{-1}. The estimated uncertainty in R is ±0.02 Å for the first shell and ±0.05 Å for outer shells; the uncertainty in N is ∼25%. [b] The goodness of the fit is defined as $F = [\sum(k^6(\chi_{exptl} - \chi_{calcd})^2)/(\sum k^6\chi_{exptl}^2)]^{1/2}$. [c] Scatterers differing by $Z \pm 1$ are not distinguishable in an EXAFS fit. The first element in a pair indicates the type of atom used to model the backscattered wave in the FEFF calculation. [d] Modeled as the Fe−N−C path of 158° of an imidazole ring.

sphere. If the first shell is modeled with two components, the short-distance component refines to a distance of 1.89 ± 0.03 Å with the coordination number of 0.5 (fit 14); a coordination number of 1.0 leads to an unreasonably high Debye−Waller factor. The distance of 1.89 Å is consistent with typical Fe^{III}−O(phenolate) bond lengths and may be attributed to coordination of Y51. If an Fe−O component at ∼1.80 Å is included in the fit, it refines to a longer ∼1.90 Å distance, consistent with the pre-edge analysis that no oxo bridge is present.

The outer-sphere scattering for oxidized DFscE11D is weak but can still be modeled with three groups of single- and multiple-scattering paths at 2.97, 3.34, and 4.18 Å (Table 6) with low coordination numbers which would correspond to scattering from a single imidazole ring. The individual contributions from these components are illustrated in k- and R'-space in Figure S11. This result quantitatively demonstrates the low intensity of the outer-shell features and suggests orientational disorder in the imidazole and carboxylate ligands. The weak intensity of outer-sphere scattering in the FT for oxidized DFscE11D contrasts with the intense outer-shell features observed for biferric complexes and proteins with short Fe−Fe distances of 3.0−3.4 Å (59−61). In these systems, there is typically at least one single-atom bridge, such as O^{2-}, OH$^-$, or OR$^-$, and additional carboxylato or alkoxo bridging groups. For example, oxidized methane monooxygenase hydroxylase contains a triply bridged bis μ-hydroxo/μ-carboxylato diiron center and displays an intense Fe−Fe peak (59). Therefore, the absence of a detectable Fe−Fe shell for oxidized DFscE11D suggests that the iron atoms are also unlikely to be bridged by a combination of hydroxo and carboxylate bridges.

DISCUSSION

From the CD titrations (Figure S1) of all DF variants, the active sites are clearly binuclear and have similar high binding affinities for ferrous ions. The excited state information derived from the NIR CD and MCD spectra of DFsc and each variant (Figure 2) indicates all possess 4C+5C biferrous active sites (56). Analysis of the VTVH MCD data shows that the ground states of these are non-Kramers doublets with $M_s = \pm 1$, an electronic configuration diagnostic of opposite signed D's and weak antiferromagnetic coupling. Weak coupling results from μ-1,3 carboxylate bridges that do not form efficient superexchange pathways. The Y51 → L substitution eliminates the 520 nm absorption

band formed by reaction with O$_2$, red shifts the 7960 cm^{-1} MCD band in biferrous DFsc (assigned as the highest energy d ← d transition of a 4C iron), and lowers the $+D$ associated with the 4C Fe^{II} (Table 2). However, this variation does not significantly affect the biferrous XAS or EXAFS spectrum below 3 Å (Figures 8 and 9). These data show that Fe1 is proximal to Y51 and that Y51 is not bound in the biferrous state. Previous resonance Raman studies showed that one Y binds to the biferric site (49). The data presented here establish that this is Y51 with an Fe^{III}−O bond length of 1.89 Å (determined from fits to the oxidized DFscE11D EXAFS). The pre-edge and EXAFS of oxidized DFscE11D also show that the biferric site does not possess an oxo bridge. Y51's influence on the LF of Fe1 likely involves an interaction with the coordinating E11 reside since they are on adjacent helices and appear to be H-bonding in the diZn NMR structure of DFsc (47). The Y51L substitution would result in a rearrangement of E11 upon elimination of the H-bond between its uncoordinated O and Y51. This would perturb the LF of the 4C iron while not significantly affecting the bond distances of the first-shell ligands (i.e., EXAFS below 3 Å, Figure 9). The carboxylate coordinated to Fe2, E44, is bidentate, consistent with the 2.55 Å feature indicative of this coordination mode observed in the FT EXAFS data (Figure 9).

The biferrous sites in various class I R2's have been shown to be 4C+5C (6, 23, 63−65). The *E. coli* R2 CD and MCD spectra are compared to the DFsc data in Figure 11. There are sign differences present in both the CD and MCD; however, the spectral shape of resolved bands and energies of the transitions are highly similar, suggesting similar geometric and electronic structures. VTVH MCD results for *E. coli* R2 show that the ground state is $M_s = \pm 2$ arising from two ferrous ions with D's of −10 and +4 cm^{-1} exchange coupled with a $J = -0.44$ cm^{-1} (6). From Figure 5 (arrows), a slight increase in the strength of antiferromagnetic coupling in DFsc results in a ground state change to $M_s = \pm 1$, as also found in the D84E R2 variant (5C+4C with $J = -1.5$ cm^{-1}) (23). Thus the GS electronic structure of the DF peptides is reminiscent of *E. coli* R2 as is the
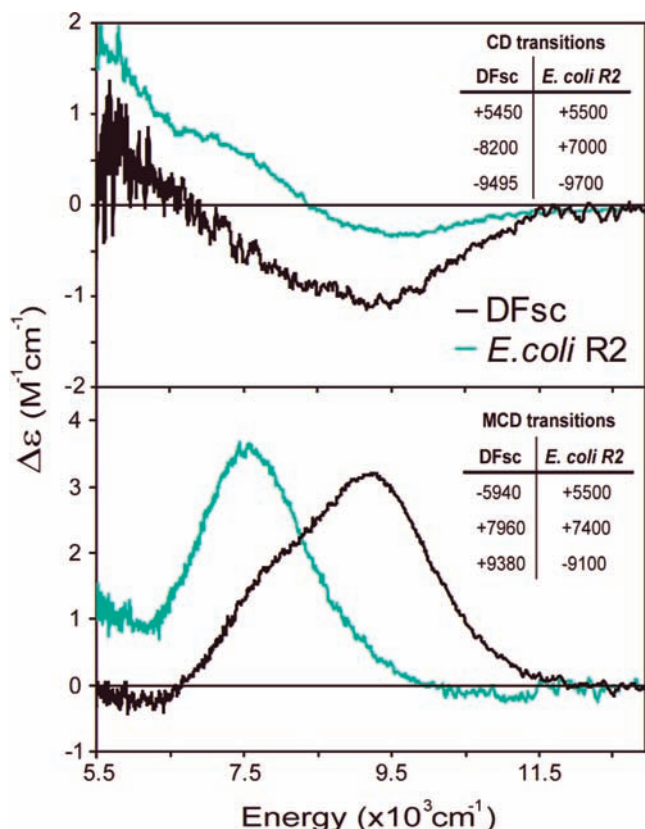
FIGURE 11: Overlay of biferrous DFsc and *E. coli* R2 CD and MCD spectra. *E. coli* R2 CD and MCD spectra and transition resolutions (sign and energy given in insets) are reproduced from ref *29*.

relatively rapid reactivity with dioxygen. Based on XAS data, this O_2 reaction directly produces a biferric site which is weakly AF coupled, from VT MCD results (*49*). (This is also supported by unpublished Mössbauer data on DFsc; R. Garcia and B. H. Huynh, personal communication.) Resonance Raman data show that a tyrosine coordinates the biferric site; however, it does not lower the potential and drive the reaction. The DFscY51L variant, where the coordinating Y residue is removed, reacts more rapidly with O_2 (5.1 s^{-1} relative to 2.1 s^{-1} in DFsc, Figure S8). Thus Y51 likely coordinates subsequent to the biferrous site's reaction with O_2. The spectroscopically determined reaction is shown in Figure 12.

Open coordination positions on each iron are required for rapid reaction with O_2. This allows dioxygen to bridge and enables 2e$^-$ transfer (one from each ferrous center) into two orthogonal antibonding orbitals on dioxygen to generate a putative peroxide level species. Computational studies on the related dimer peptide (DF2t) show that a peroxo species formed by 2e$^-$ transfer (one from each Fe^{II}) is the most energetically favorable pathway (*45*). Thus 4C+5C biferrous sites are poised for rapid reaction with oxygen. Indeed,

biferrous MMOH and Δ^9D, which lack properly oriented open coordination positions on both irons, do not react rapidly with oxygen. Furthermore, the second open coordination position on the 4C iron provides a site for Y51 to bind along the reaction coordinate. Y18, which is a similar distance from the diiron site, is sterically prevented from binding to its proximal iron since, at the putative peroxo level, this iron should be coordinatively saturated due to the bidentate carboxylate. Binding of Y51 functions as an internal spectral probe of the O_2 reaction and would serve as a proton source to accelerate decay of the putative peroxo intermediate. In the absence of Y51 (i.e., DFscY51L), water could bind to the second open coordination position on the 4C center and also function as a proton source as the site is solvent exposed. An additional properly oriented open coordination position on one iron and the availability of a proton source (endogenous or H_2O) could be a structural mechanism used by natural binuclear iron enzymes to drive the reaction past the biferric peroxo level intermediate. Peroxo intermediates have been identified in oxygen reactions of ferritin (*15*) (5C+5C), Δ^9D with substrate (*4, 13*) (4C+5C), the MMOH/component B complex (*66*) (5C+5C), and the D84E variant (*26*) of *E. coli* R2 (5C+4C). The intermediates from D84E-R2 and Δ^9D are more stable than those observed in ferritin and MMOH. D84E substitution in R2 changes the 4C+5C R2 site to 5C+4C and thus alters solvent access to the open coordination position (*23*), while the site in Δ^9D is believed to have limited solvent access (*67*). In MMOH and ferritin, water molecules are already bound to the sites at the biferrous level and could provide a proton leading to the lowered stability of these intermediates.

The DFsc four-helix bundle is ideal for systematic ground-up studies to elucidate the factors that tune diiron sites for differential oxygen reactivity, as observed in nature. The current generation binds Fe^{II} with high affinity to create a binuclear active site with spectral properties very similar to R2, react with oxygen rapidly like R2, and generate a biferric product site (though not oxo-bridged as in R2). This is considerable progress in *de novo* design, and the next step is to stabilize intermediates. Removal of the internal proton source Y51 did not stabilize an intermediate because the sites are still highly solvent accessible. Thus H_2O access to the site needs to be regulated, or external proton sources need to be removed. The E11D variation kinetically affected Fe^{II} loading while not perturbing O_2 reactivity (access) and shows that, in principle, selective discrimination at the active site is feasible. Also, these relatively small peptides are soluble in various nonaqueous solvents. Currently, a number of approaches are being explored to trap the peroxo species in these *de novo* designed peptides and evaluate the factors that promote further reactivity.
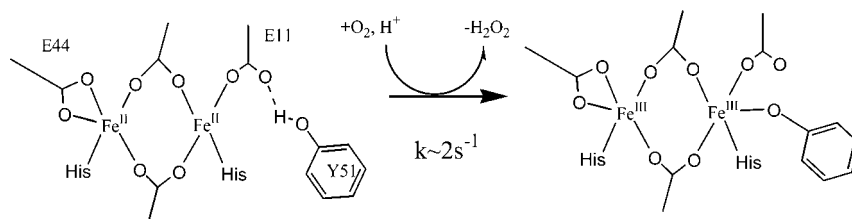

FIGURE 12: Spectroscopically derived DFsc O_2 reaction.

Bell et al.

SUPPORTING INFORMATION AVAILABLE

CD titrations, VTVH MCD overlays and simulations, EXAFS fits, and kinetic traces for DFsc and variants. This material is available free of charge via the Internet at http://pubs.acs.org.

REFERENCES

1. Solomon, E. I., Brunold, T. C., Davis, M. I., Kemsley, J. N., Lee, S. K., Lehnert, N., Neese, F., Skulan, A. J., Yang, Y. S., and Zhou, J. (2000) Geometric and electronic structure/function correlations in non-heme iron enzymes. *Chem. Rev. 100*, 235–350.
2. Wallar, B. J., and Lipscomb, J. D. (1996) Dioxygen activation by enzymes containing binuclear non-heme iron clusters. *Chem. Rev. 96*, 2625–2658.
3. Bollinger, J. M., Jr., Tong, W. H., Ravi, N., Huynh, B. H., Edmondson, D. E., and Stubbe, J. A. (1995) Use of rapid kinetics methods to study the assembly of the diferric-tyrosyl radical cofactor of *E. coli* ribonucleotide reductase. *Methods Enzymol. 258*, 278–303.
4. Broadwater, J. A., Ai, J., Loehr, T. M., Sanders-Loehr, J., and Fox, B. G. (1998) Peroxodiferric intermediate of stearoyl-acyl carrier protein Δ^9 desaturase: oxidase reactivity during single turnover and implications for the mechanism of desaturation. *Biochemistry 37*, 14664–14671.
5. Lipscomb, J. D. (1994) Biochemistry of the soluble methane monooxygenase. *Annu. Rev. Microbiol. 48*, 371–399.
6. Yang, Y. S., Baldwin, J., Ley, B. A., Bollinger, J. M., Jr., and Solomon, E. I. (2000) Spectroscopic and electronic structure description of the reduced binuclear non-heme iron active site in ribonucleotide reductase from *E. coli*: comparison to reduced Δ^9 desaturase and electronic structure contributions to differences in O_2 reactivity. *J. Am. Chem. Soc. 122*, 8495–8510.
7. Yang, Y.-S., Broadwater, J. A., Pulver, S. C., Fox, B. G., and Solomon, E. I. (1999) Circular dichroism and magnetic circular dichroism studies of the reduced binuclear non-heme iron site of stearoyl-ACP Δ^9-desaturase: substrate binding and comparison to ribonucleotide reductase. *J. Am. Chem. Soc. 121*, 2770–2783.
8. Rosenzweig, A. C., Brandstetter, H., Whittington, D. A., Nordlund, P., Lippard, S. J., and Frederick, C. A. (1997) Crystal structures of the methane monooxygenase hydroxylase from *Methylococcus capsulatus* (Bath): implications for substrate gating and component interactions. *Proteins 29*, 141–152.
9. Whittington, D. A., and Lippard, S. J. (2001) Crystal structures of the soluble methane monooxygenase hydroxylase from *Methylococcus capsulatus* (Bath) demonstrating geometrical variability at the dinuclear iron active site. *J. Am. Chem. Soc. 123*, 827–838.
10. Yoon, S., and Lippard, S. J. (2005) Water affects the stereochemistry and dioxygen reactivity of carboxylate-rich diiron(II) models for the diiron centers in dioxygen-dependent non-heme enzymes. *J. Am. Chem. Soc. 127*, 8386–8397.
11. Mitic, N., Schwartz, J. K., Lipscomb, J. D., and Solomon, E. I. (2008) CD and MCD studies of the effects of component B variant binding on the biferrous active site of methane monooxygenase. *Biochemistry* (in press).
12. Pulver, S. C., Froland, W. A., Lipscomb, J. D., and Solomon, E. I. (1997) Ligand field circular dichroism and magnetic circular dichroism studies of component B and substrate binding to the hydroxylase component of methane monooxygenase. *J. Am. Chem. Soc. 119*, 387–395.
13. Broadwater, J. A., Achim, C., Münck, E., and Fox, B. G. (1999) Mossbauer studies of the formation and reactivity of a quasi-stable peroxo intermediate of stearoyl-acyl carrier protein Δ^9-desaturase. *Biochemistry 38*, 12197–12204.
14. Kurtz, D. M., Jr. (1997) Structural similarity and functional diversity in diiron-oxo proteins. *J. Biol. Inorg. Chem. 2*, 159–167.
15. Moënne-Loccoz, P., Krebs, C., Herlihy, K., Edmondson, D. E., Theil, E. C., Huynh, B. H., and Loehr, T. M. (1999) The ferroxidase reaction of ferritin reveals a diferric μ-1,2 bridging peroxide intermediate in common with other O_2-activating non-heme diiron proteins. *Biochemistry 38*, 5290–5295.
16. Yun, D., Garcia-Serres, R., Chicalese, B. M., An, Y. H., Huynh, B. H., and Bollinger, J. M. (2007) (μ-1,2-peroxo)diiron(III/III) complex as a precursor to the diiron(III/IV) intermediate X in the assembly of the iron-radical cofactor of ribonucleotide reductase from mouse. *Biochemistry 46*, 1925–1932.
17. Skulan, A. J., Brunold, T. C., Baldwin, J., Saleh, L., Bollinger, J. M., Jr., and Solomon, E. I. (2004) Nature of the peroxo intermediate of the W48F/D84E ribonucleotide reductase variant: implications for O_2 activation by binuclear non-heme iron enzymes. *J. Am. Chem. Soc. 126*, 8842–8855.
18. Beauvais, L. G., and Lippard, S. J. (2005) Reactions of the peroxo intermediate of soluble methane monooxygenase hydroxylase with ethers. *J. Am. Chem. Soc. 127*, 7370–7378.
19. Sturgeon, B. E., Burdi, D., Chen, S., Huynh, B. H., Edmondson, D. E., Stubbe, J., and Hoffman, B. M. (1996) Reconsideration of X, the diiron intermediate formed during cofactor assembly in *E. coli* ribonucleotide reductase. *J. Am. Chem. Soc. 118*, 7551–7557.
20. Mitic, N., Clay, M. D., Saleh, L., Bollinger, J. M., Jr., and Solomon, E. I. (2007) Spectroscopic and electronic structure studies of intermediate X in ribonucleotide reductase R2 and two variants: a description of the Fe^{IV}-oxo bond in the Fe^{III}-O-Fe^{IV} dimer. *J. Am. Chem. Soc. 129*, 9049–9065.
21. Shu, L., Nesheim, J. C., Kauffmann, K., Münck, E., Lipscomb, J. D., and Que, L. (1997) An $Fe^{IV}_2O_2$ diamond core structure for the key intermediate Q of methane monooxygenase. *Science 275*, 515–518.
22. Brazeau, B. J., and Lipscomb, J. D. (2000) Kinetics and activation thermodynamics of methane monooxygenase compound Q formation and reaction with substrates. *Biochemistry 39*, 13503–13515.
23. Wei, P. P., Skulan, A. J., Mitic, N., Yang, Y. S., Saleh, L., Bollinger, J. M., Jr., and Solomon, E. I. (2004) Electronic and spectroscopic studies of the non-heme reduced binuclear iron sites of two ribonucleotide reductase variants: comparison to reduced methane monooxygenase and contributions to O_2 reactivity. *J. Am. Chem. Soc. 126*, 3777–3788.
24. Logan, D. T., deMare, F., Persson, B. O., Slaby, A., Sjöberg, B. M., and Nordlund, P. (1998) Crystal structures of two self-hydroxylating ribonucleotide reductase protein R2 mutants: structural basis for the oxygen-insertion step of hydroxylation reactions catalyzed by diiron proteins. *Biochemistry 37*, 10798–10807.
25. Tong, W., Burdi, D., Riggs-Gelasco, P., Chen, S., Edmondson, D., Huynh, B. H., Stubbe, J., Han, S., Arvai, A., and Tainer, J. (1998) Characterization of Y122F R2 of *Escherichia coli* ribonucleotide reductase by time-resolved physical biochemical methods and X-ray crystallography. *Biochemistry 37*, 5840–5848.
26. Moënne-Loccoz, P., Baldwin, J., Ley, B. A., Loehr, T. M., and Bollinger, J. M. (1998) O_2 activation by non-heme diiron proteins: identification of a symmetric μ-1,2-peroxide in a mutant of ribonucleotide reductase. *Biochemistry 37*, 14659–14663.
27. Saleh, L., Krebs, C., Ley, B. A., Naik, S., Huynh, B. H., and Bollinger, J. M. (2004) Use of a chemical trigger for electron transfer to characterize a precursor to cluster X in assembly of the iron-radical cofactor of *Escherichia coli* ribonucleotide reductase. *Biochemistry 43*, 5953–5964.
28. Baldwin, J., Voegtli, W. C., Khidekel, N., Moënne-Loccoz, P., Krebs, C., Pereira, A. S., Ley, B. A., Huynh, B. H., Loehr, T. M., Riggs-Gelasco, P. J., Rosenzweig, A. C., and Bollinger, J. M. (2001) Rational reprogramming of the R2 subunit of *Escherichia coli* ribonucleotide reductase into a self-hydroxylating monooxygenase. *J. Am. Chem. Soc. 123*, 7017–7030.
29. Zhao, M., Song, D., and Lippard, S. J. (2006) Water induces a structural conversion and accelerates the oxygenation of carboxylate-bridged non-heme diiron enzyme synthetic analogues. *Inorg. Chem. 45*, 6323–6330.
30. Sazinsky, M. H., and Lippard, S. J. (2006) Correlating structure with function in bacterial multicomponent monooxygenases and related diiron proteins. *Acc. Chem. Res. 39*, 558–566.
31. Que, L., Jr., and Tolman, W. B. (2002) Bis(μ-oxo)dimetal "diamond" cores in copper and iron complexes relevant to biocatalysis. *Angew. Chem., Int. Ed. Engl. 41*, 1114–1137.
32. Skulan, A. J., Hanson, M. A., Hsu, H. F., Que, L., Jr., and Solomon, E. I. (2003) Spectroscopic study of [Fe₂O₂(5-Et3-TPA) ₂]³⁺: nature of the Fe_2O_2 diamond core and its possible relevance to high-valent binuclear non-heme enzyme intermediates. *J. Am. Chem. Soc. 125*, 7344–7356.
33. Xue, G., Wang, D., De Hont, R., Fiedler, A. T., Shan, X., Münck, E., and Que, L. (2007) A synthetic precedent for the [$Fe^{IV}_2(\mu$-O) ₂] diamond core proposed for methane monooxygenase intermediate Q. *Proc. Natl. Acad. Sci. U.S.A. 104*, 20713–20718.
34. Tshuva, E. Y., and Lippard, S. J. (2004) Synthetic models for non-heme carboxylate-bridged diiron metalloproteins: strategies and tactics. *Chem. Rev. 104*, 987–1012.
35. Yamashita, M., Furutachi, H., Tosha, T., Fujinami, S., Saito, W., Maeda, Y., Takahashi, K., Tanaka, K., Kitagawa, T., and Suzuki,

M. (2007) Regioselective arene hydroxylation mediated by a (μ-peroxo)diiron(III) complex: a functional model for toluene monooxygenase. *J. Am. Chem. Soc. 129*, 2–3.

36. Kurtz, D. M. (1989) Oxo- and hydroxo-bridged diiron complexes: a chemical perspective on a biological unit. *Chem. Rev. 90*, 585–606.

37. Solomon, E. I., Tuczek, F., Root, D. E., and Brown, C. A. (1994) Spectroscopy of binuclear dioxygen complexes. *Chem. Rev. 94*, 827–856.

38. Di Costanzo, L., Wade, H., Geremia, S., Randaccio, L., Pavone, V., DeGrado, W. F., and Lombardi, A. (2001) Toward the de novo design of a catalytically active helix bundle: a substrate-accessible carboxylate-bridged dinuclear metal center. *J. Am. Chem. Soc. 123*, 12749–12757.

39. Lombardi, A., Summa, C. M., Geremia, S., Randaccio, L., Pavone, V., and DeGrado, W. F. (2000) Inaugural article: retrostructural analysis of metalloproteins: application to the design of a minimal model for diiron proteins. *Proc. Natl. Acad. Sci. U.S.A. 97*, 6298–6305.

40. Hill, R. B., Raleigh, D. P., Lombardi, A., and DeGrado, W. F. (2000) De novo design of helical bundles as models for understanding protein folding and function. *Acc. Chem. Res. 33*, 745–754.

41. DeGrado, W. F. (1997) Proteins from scratch. *Science 278*, 80–81.

42. Kaplan, J., and DeGrado, W. F. (2004) De novo design of catalytic proteins. *Proc. Natl. Acad. Sci. U.S.A. 101*, 11566–11570.

43. Calhoun, J. R., Nastri, F., Maglio, O., Pavone, V., Lombardi, A., and Degrado, W. F. (2005) Artificial diiron proteins: From structure to function. *Biopolymers 80*, 264–278.

44. Wade, H., Stayrook, S. E., and Degrado, W. F. (2006) The structure of a designed diiron(III) protein: implications for cofactor stabilization and catalysis. *Angew. Chem., Int. Ed. Engl. 45*, 4951–4954.

45. Wei, P. P., Skulan, A. J., Wade, H., DeGrado, W. F., and Solomon, E. I. (2005) Spectroscopic and computational studies of the de novo designed protein DF2t: correlation to the biferrous active site of ribonucleotide reductase and factors that affect O_2 reactivity. *J. Am. Chem. Soc. 127*, 16098–16106.

46. Calhoun, J. R., Kono, H., Lahr, S., Wang, W., DeGrado, W. F., and Saven, J. G. (2003) Computational design and characterization of a monomeric helical dinuclear metalloprotein. *J. Mol. Biol. 334*, 1101–1115.

47. Calhoun, J. R., Liu, W., Spiegel, K., Dal Peraro, M., Klein, M. L., Valentine, K. G., Wand, A. J., and DeGrado, W. F. (2008) Solution NMR structure of a designed metalloprotein and complementary molecular dynamics refinement. *Structure 16*, 210–215.

48. Summa, C. M., Lombardi, A., Lewis, M., and DeGrado, W. F. (1999) Tertiary templates for the design of diiron proteins. *Curr. Opin. Struct. Biol. 9*, 500–508.

49. Calhoun, J. R., Bell, C. B., Smith, T. J., Thamann, T. J., DeGrado, W. F., and Solomon, E. I. (2008) Oxygen reactivity of the biferrous site in the de novo designed four helix bundle peptide DFsc: nature of the "904 intermediate" and reaction mechanism. *J. Am. Chem. Soc.* (in press).

50. Solomon, E. I., Pavel, E. G., Loeb, K. E., and Campochiaro, C. (1995) Magnetic circular dichroism spectroscopy as a probe of the geometric and electronic structure of non-heme ferrous enzymes. *Coord. Chem. Rev. 144*, 369–460.

51. Lear, J. D., DeGrado, W. F., and Calhoun, J. R. (2003) Computational design and characterization of a monomeric helical dinuclear metalloprotein. *Proc. Natl. Acad. Sci. U.S.A. 100*, 14772–14777.

52. Neese, F., and Solomon, E. I. (1999) MCD C-term signs, saturation behavior, and determination of band polarizations in randomly oriented systems with spin $S \geq 1/2$. Applications to $S = 1/2$ and $S = 5/2$. *Inorg. Chem. 38*, 1847–1865.

53. Ellis, P. J., and Freeman, H. C. (1995) Xfit—an interactive EXAFS analysis program. *J. Synchrotron Radiat. 2*, 190–195.

54. Ankudinov, A. L., and Rehr, J. J. (1997) Relativistic calculations of spin-dependent x-ray-absorption spectra. *Phys. Rev. B 56*, R1712–R1715.

55. Westre, T. E., Kennepohl, P., DeWitt, J. G., Hedman, B., Hodgson, K. O., and Solomon, E. I. (1997) A multiplet analysis of Fe K-edge 1s→3d pre-edge features of iron complexes. *J. Am. Chem. Soc. 119*, 6297–6314.

56. Reem, R. C., and Solomon, E. I. (1987) Spectroscopic studies of the binuclear ferrous active site of deoxyhemerythrin: coordination number and probable bridging ligands for the native and ligand bound forms. *J. Am. Chem. Soc. 109*, 1216–1226.

57. Pavel, E. G., Kitajima, N., and Solomon, E. I. (1998) Magnetic circular dichroism spectroscopic studies of mononuclear non-heme ferrous model complexes. Correlation of excited- and ground-state electronic structure with geometry. *J. Am. Chem. Soc. 120*, 3949–3962.

58. Riggs-Gelasco, P. J., Stemmler, T. L., and Penner-Hahn, J. E. (1995) XAFS of dinuclear metal sites in proteins and model compounds. *Coord. Chem. Rev. 144*, 245–286.

59. Rudd, D. J., Sazinsky, M. H., Merkx, M., Lippard, S. J., Hedman, B., and Hodgson, K. O. (2004) Determination by X-ray absorption spectroscopy of the Fe-Fe separation in the oxidized form of the hydroxylase of methane monooxygenase alone and in the presence of MMOD. *Inorg. Chem. 43*, 4579–4589.

60. Hedman, B., Co, M. S., Armstrong, W. H., Hodgson, K. O., and Lippard, S. J. (1986) EXAFS studies of binuclear iron complexes as models for hemerythrin and related proteins. *Inorg. Chem. 25*, 3708–3711.

61. Slep, L. D., Mijovilovich, A., Meyer-Klaucke, W., Weyhermuller, T., Bill, E., Bothe, E., Neese, F., and Wieghardt, K. (2003) Mixed-valent [Fe^{IV}(μ-O)(μ-carboxylato) $_2$Fe^{III}]$^{3+}$ core. *J. Am. Chem. Soc. 125*, 15554–15570.

62. Deleted in proof.

63. Strand, K. R., Yang, Y. S., Andersson, K. K., and Solomon, E. I. (2003) Circular dichroism and magnetic circular dichroism studies of the biferrous form of the R2 subunit of ribonucleotide reductase from mouse: comparison to the R2 from *Escherichia coli* and other binuclear ferrous enzymes. *Biochemistry 42*, 12223–12234.

64. Wei, P. P., Tomter, A. B., Rohr, A. K., Andersson, K. K., and Solomon, E. I. (2006) Circular dichroism and magnetic circular dichroism studies of the active site of p53R2 from human and mouse: Iron binding and nature of the biferrous site relative to other ribonucleotide reductases. *Biochemistry 45*, 14043–14051.

65. Tomter, A. B., Bell, C. B., Rohr, A. K., Andersson, K. K., and Solomon, E. I. (2008) Circular dichroism and magnetic circular dichroism studies of the biferrous site of the class Ib ribonucleotide reductase from *Bacillus cereus*: comparison to the class Ia enzymes. *Biochemistry* (in press).

66. Lee, S. K., Nesheim, J. C., and Lipscomb, J. D. (1993) Transient intermediates of the methane monooxygenase catalytic cycle. *J. Biol. Chem. 268*, 21569–21577.

67. Lindqvist, Y., Huang, W., Schneider, G., and Shanklin, J. (1996) Crystal structure of Δ^9 stearoyl-acyl carrier protein desaturase from castor seed and its relationship to other di-iron proteins. *EMBO J. 15*, 4081–4092.